

## A generalised stochastic backscatter model

O'Neill, James; Cai, Xiaoming; Kinnersley, Robert

DOI:

[10.1002/qj.2548](https://doi.org/10.1002/qj.2548)

License:

Other (please specify with Rights Statement)

Document Version

Peer reviewed version

Citation for published version (Harvard):

O'Neill, J, Cai, X & Kinnersley, R 2015, 'A generalised stochastic backscatter model: large-eddy simulation of the neutral surface layer', *Quarterly Journal of the Royal Meteorological Society*, vol. 141, no. 692, pp. 2617–2629. <https://doi.org/10.1002/qj.2548>

[Link to publication on Research at Birmingham portal](#)

### Publisher Rights Statement:

This is the accepted version of the following article: O'Neill, J. J., X-M. Cai, and R. Kinnersley. "A generalised stochastic backscatter model: large-eddy simulation of the neutral surface layer." *Quarterly Journal of the Royal Meteorological Society* (2015)., which has been published in final form at: <http://dx.doi.org/10.1002/qj.2548>.

Eligibility for repository checked May 2015

### General rights

Unless a licence is specified above, all rights (including copyright and moral rights) in this document are retained by the authors and/or the copyright holders. The express permission of the copyright holder must be obtained for any use of this material other than for purposes permitted by law.

- Users may freely distribute the URL that is used to identify this publication.
- Users may download and/or print one copy of the publication from the University of Birmingham research portal for the purpose of private study or non-commercial research.
- User may use extracts from the document in line with the concept of 'fair dealing' under the Copyright, Designs and Patents Act 1988 (?)
- Users may not further distribute the material nor use it for the purposes of commercial gain.

Where a licence is displayed above, please note the terms and conditions of the licence govern your use of this document.

When citing, please reference the published version.

### Take down policy

While the University of Birmingham exercises care and attention in making items available there are rare occasions when an item has been uploaded in error or has been deemed to be commercially or otherwise sensitive.

If you believe that this is the case for this document, please contact [UBIRA@lists.bham.ac.uk](mailto:UBIRA@lists.bham.ac.uk) providing details and we will remove access to the work immediately and investigate.

# A generalised stochastic backscatter model: large-eddy simulation of the neutral surface layer

---

J.J. O'Neill<sup>1</sup>, X.-M. Cai<sup>2</sup> and R. Kinnersley<sup>3</sup>

<sup>1,2</sup>School of Geography, Earth and Environmental Sciences, University of Birmingham, Edgbaston, Birmingham, B15 2TT

<sup>3</sup>Environment Agency, Horizon House, Deanery Road, Bristol, BS1 5AH

<sup>2</sup>Email: x.cai@bham.ac.uk

## Abstract

The Smagorinsky subgrid model remains popular in large-eddy simulation (LES) modelling despite its failure to reproduce mean velocity shear within the atmospheric surface layer. Over-predictions as large as 100% are not uncommon, leading to local simulation degradation and potentially infecting scales further from the surface. Mason and Thomson achieved significant reduction in excessive velocity shear by adding stochastic accelerations on top of the Smagorinsky model to account for backscattered energy from the subgrid scales. However, neither this model nor its later implementation by Weinbrecht and Mason are able to ensure a physically appropriate spatial structure for the backscatter acceleration fields throughout the domain: with the Mason and Thomson model, the backscatter length scale and anisotropy depend on the local grid spacing and aspect ratio; with the Weinbrecht and Mason model, the backscatter is unavoidably isotropic with uniform length scale. We propose a new method for the generation of stochastic backscatter acceleration fields which utilises a grid-adaptive filter (GAF) capable of *controlling spatial variations in the backscatter length scale and anisotropy, independently of the model grid*. When applied to the atmospheric surface layer, this allows for the backscatter length scale to be reduced

towards surfaces in an appropriate manner, and the backscatter anisotropy to be varied in accordance with the physical anisotropy of the subgrid scales. The GAF model also has wider applicability; it may be used when the LES filter width, and hence the backscatter length scale, varies spatially with local 3-D grid refinement. The GAF model is initially tested for the case of LES of the neutral atmospheric boundary layer, for grid aspect ratios ranging from  $\alpha = \Delta x / \Delta z = 1$  to 10, and found to give a reduction in maximum excessive mean velocity shear (from that obtained without backscatter) of around 80%, that is largely independent of  $\alpha$ .

**Keywords:** Discrete filter; Large-eddy simulation; Near-wall modelling; Neutral surface layer; Refined grids; Stochastic backscatter.

## 1. Introduction

Parameterisations that impose stochastic fluctuations in the subgrid-scale (SGS) stresses, in order to model backscatter from the unresolved scales, are now used by a wide range atmospheric models due to their associated benefits. For example, in general circulation models, they have led to improvements in Rossby wave and baroclinic flow simulations as a result of better representation of energy spectra (Zidikheri and Frederiksen, 2009, Frederiksen and Davies, 1997). In ensemble numerical weather prediction models, they remove the need for arbitrary perturbation of the initial condition in order to generate ensemble member spread, and may even lead to improvements in forecast skill (Palmer *et al.*, 2009, Shutts, 2005). In large-eddy simulation (LES) modelling, Leith (1990) found that his random fluctuations provided the natural seeds from which large-scale turbulent structures grew, and Mason and Thomson (1992) later used a similar scheme to significantly improve the prediction of mean velocity shear within the atmospheric surface layer.

The forward scatter (towards smaller scales) and backscatter (towards larger scales) of energy within a turbulent flow are often large and comparable in magnitude (Westbury *et al.*, 2004). Despite this, the majority of SGS parameterisations used in LES modelling are purely dissipative, implying that they seek to represent the net energy transfer rather than the forward and backward scatter separately (Leslie and Quarini, 1979). This is typically achieved through a ‘net’ eddy-viscosity, whose magnitude follows from a local energy balance equation in which quantities on the smallest resolved scales are used to facilitate closure, e.g. the Smagorinsky (1963) model. In well resolved cases the energy carried by the subgrid turbulence scales accounts for a small portion (the value of which depends on the grid resolution adopted) of the total available energy and previous studies have indicated that simulation performance is largely unaffected by the choice of SGS model in such cases (Mason, 1994). In less well-resolved cases, however, the SGS model carries a more appreciable fraction of the available energy, and the potential consequences of a lack of modelled backscatter can be more severe. Poorly resolved LES should therefore be avoided. However, with limited computational resources, this is not always possible, for example in simulations of strongly stable flow or flow close to solid surfaces, where the characteristic length scale of the largest eddies is small (Mason, 1994).

Numerous LES studies of the atmospheric boundary layer (ABL) have shown that SGS models that do not account for backscatter almost invariably lead to over-prediction of near-surface velocity shear (Michioka and Chow, 2008, Kirkil *et al.*, 2012, Mason and Thomson, 1992, Talbot *et al.*, 2012). In the neutral surface layer, this is seen as a deviation from the expected logarithmic velocity profile. Brasseur and Wei (2010) refer to this as the “overshoot” issue, and provide several further examples of studies in which this issue has been observed. Despite being localised to the near-surface region, any associated simulation deficiencies can be fed up into, and subsequently infect, the larger turbulent length scales

away from the surface, leading to further deterioration in simulation accuracy (Chamecki, 2010). In the surface layer itself, these errors will directly affect the transportation and dispersion of fluxes and scalars, to the detriment of, for example, pollution dispersion models driven by LES fields. This has led to the formulation of a variety of SGS models in which backscatter is considered. These models may be categorised into one of two types: deterministic and stochastic.

Deterministic models that consider the effect of backscatter include those from the ‘dynamic’ family, pioneered by Germano *et al.* (1991), which allow the constant in an eddy viscosity model to vary in space and time depending on the local flow behaviour of the smallest-resolved scales. A reduced model constant close to the surface essentially allows for more mixing of momentum and a corresponding reduction in vertical velocity shear. However, ‘true’ backscatter can only be explicitly represented in such models through a locally negative eddy-viscosity, whereas this is typically prohibited in practice as it can lead to the growth of flow instabilities (Kirkil *et al.*, 2012). Dynamic models might therefore be said to allow for ‘partial’ rather than ‘full’ energy backscatter, which cannot be simulated with reduced eddy viscosities alone (Schumann, 1995). Other deterministic models allowing for backscatter have also been formulated (Chow *et al.*, 2005, Kosovic, 1997, Domaradzki and Saiki, 1997); however their ability to fully remove discrepancies in the turbulence statistics of wall-bounded flows remains elusive.

Stochastic models, on the other hand, are able to model backscatter directly by imposing random fluctuations in the subgrid stresses that inject energy into the flow at the smallest resolved scales, e.g. Schumann (1995). Leith (1990) simulated a plane shear mixing layer by superimposing non-divergent random accelerations on top of the Smagorinsky SGS model. The stochastic backscatter model of Mason and Thomson (1992) (hereafter, MT92) extended this idea to be more applicable to LES of the ABL. This model proved remarkably successful

in reducing the excessive velocity shear within the neutral surface layer as seen with the Smagorinsky model alone. However, the model was initially formulated on the assumption of the computational grid mesh being fairly isotropic. When generating the backscatter acceleration fields, a 3-D 1:2:1 spatial filter is applied to white-noise fields, generated on the model grid, in order to introduce a backscatter length scale that scales with the LES filter width. However, in areas of high vertical grid refinement (for example) the backscatter length scale in the wall-normal direction is reduced, which causes an inappropriately high level of anisotropy to be introduced into the backscatter acceleration fields. Practically, this adds disproportionately large backscatter signals to the flow-field in the horizontal, and little in the vertical, leading to a reduction in the ability of the backscatter model to enhance vertical momentum flux so as to smooth out vertical velocity gradients within the surface layer. To alleviate such issues, Weinbrecht and Mason (2008) (hereafter, WM08) later proposed a modification to the MT92 model, in which the white-noise fields are instead generated and filtered on a secondary isotropic grid, with resolution scaled on the LES filter width in the interior of the simulated ABL, and then linearly interpolated onto the anisotropic model grid. This method imposes that the backscatter length scale is fixed and spatially isotropic, which, unlike the MT92 model, ensures a largely grid-independent reduction in excessive velocity shear. However, as discussed below, such spatial uniformity in the backscatter acceleration fields is not always physically appropriate; furthermore, the applicability of the model is limited to simple grid geometries in which the LES filter width is assumed fixed throughout the domain.

LES is based on the assumption that the filter operation separates the large anisotropic eddies, responsible for most of the turbulent energy transport, from the small isotropic eddies, responsible for most of the turbulent energy dissipation. With the Smagorinsky SGS model, the LES filter width is assumed to scale with the local grid mesh size. Thus in well-resolved

interior regions of the flow, one can expect the backscatter from the unresolved scales to be fairly isotropic and grid-scale. However, as the surface is approached, the local turbulence production length scale approaches (and eventually falls below) the LES filter width, and the assumption of isotropy in the subgrid scales is no longer appropriate. In this near-surface region, one would also expect the backscatter anisotropy to vary in accordance with the physical anisotropy of the subgrid scales, and the backscatter length scale to reduce with the turbulence production length scale once it falls below the grid scale. Unfortunately, the lack of control over the local backscatter length scale and anisotropy with the MT92 and WM08 models means that such a characteristic spatial structure is unachievable, prompting an alternative method to be sought for the generation of the backscatter acceleration fields.

At the same time, the ability to control the backscatter length scale would also widen the applicability of the backscatter model to LES studies of more complex flow geometries, for example in many urban or engineering flow setups, which make use of local 3-dimensional grid refinement (in contrast to vertical grid stretching alone) in order to ensure computationally efficient resolution of the most important turbulence length scales. Indeed, even the comparatively simple geometries associated with horizontally homogeneous boundary-layer flow require the resolution of a multitude of scales for accurate simulation, and adaptive mesh refinement techniques have often been adopted in such cases (Vanella *et al.*, 2008). Since, with the Smagorinsky model, a locally refined grid mesh implies a spatially varying LES filter width, the backscatter length scale should also vary in accordance with the local LES filter width. Whilst this requirement is fairly well met with the MT92 model's filtering procedure, with the WM08 model, the backscatter length scale remains fixed at the scale of the secondary isotropic grid. For nested grids (i.e. sudden grid refinement) it might be possible to define a separate isotropic grid within each sub-domain; however, in order to minimise associated commutation errors, the LES filter width is typically varied gradually,

either by employing gradual grid refinement (Kravchenko *et al.*, 1996) or by using an explicit filter to decouple the LES filter width from the grid mesh size, which can then be varied smoothly across grid discontinuities (Piomelli *et al.*, 2006). In this case, the WM08 model could not ensure a physically appropriate backscatter length scale everywhere.

In this paper, we develop a new method for generating stochastic backscatter acceleration fields that allows the local backscatter length scale and anisotropy to be controlled independently of the model grid. The backscatter length scale can then be reduced appropriately towards surfaces, and, if necessary, varied to reflect any spatial variations in LES filter width, and the backscatter anisotropy can be specified in relation to the physical anisotropy of the subgrid scales. The advantages of the new model, and the corresponding limitations of the MT92 and WM08 models, are illustrated in the schematic diagram in Figure 1, which shows an example case in which the LES filter width decreases towards the bottom right corner of the domain as drawn (as a result of smooth grid refinement). It can be seen that in the flow interior, the backscatter is appropriately grid-scale and isotropic for all three models, except for the MT92 model in areas of horizontal grid refinement, where the backscatter becomes unphysically anisotropic due to the dependence of the 1:2:1 filter operation on the local grid spacing. Closer to the surface, the backscatter anisotropy with the new model is increased gradually in accordance with an assumed profile of the physical anisotropy of the subgrid scales. With the MT92 model, however, the dependence of the anisotropy on the grid spacing results in regions of unphysically high or unphysically low anisotropy, and with the WM08 model, the backscatter remains isotropic at all distances from the surface. With the new model, the backscatter length scale is reduced towards the surface in accordance with the local subgrid turbulence length scale, and further reduced in refined grid regions to reflect the reduced LES filter width, whereas the length scale remains fixed at



the local grid scale with the MT92 model, and fixed at the coarse grid scale with the WM08 model (resulting in particularly unphysically large structures in the highest refined region).

This paper is structured as follows. Section 2 gives details of the stochastic backscatter model and the new method for generating the backscatter acceleration fields. The new model is then tested along with the MT92 and WM08 models for the case of LES of the neutral atmospheric boundary layer, on a number of different grid meshes with varying degrees of vertical grid refinement (more complex grid geometries will be tackled in future work), with assessment of the prediction of mean velocity shear within the surface layer; Section 3 describes the various LES configurations and Section 4 presents the results and provides discussion. Finally, conclusions are drawn in Section 5.

## 2. The stochastic backscatter model

### 2.1. Foundations

The stochastic backscatter model is based on the concept of imposing pseudo-random acceleration fields on top of the LES acceleration fields obtained using the Smagorinsky SGS model (Mason and Thomson, 1992):

$$\frac{\partial u_i}{\partial t} = \dots + \frac{\partial}{\partial x_j} \left\{ v_{\text{sgs}} \left( \frac{\partial u_i}{\partial x_j} + \frac{\partial u_j}{\partial x_i} \right) \right\} + a_i, \quad (1)$$

sum over  $j = 1, 2, 3$ , where  $u_i = \{u, v, w\}$  is the LES (filtered) velocity field,  $t$  is time,  $x_i = \{x, y, z\}$  is a Cartesian coordinate system,  $v_{\text{sgs}}$  is a subgrid-scale eddy-viscosity,  $a_i = \{a_1, a_2, a_3\}$  is a backscatter acceleration field, and the ellipsis signifies all the other terms in the adopted LES momentum equation (advection, pressure gradient, Coriolis force, etc.)

Each backscatter acceleration field must be appropriately scaled to inject the desired amount of energy into the LES field, and should ideally be divergence-free. The general procedure for obtaining a backscatter acceleration field is as follows:

- (i) Generate three gridded fields of uniformly distributed random numbers with zero mean and unit variance,  $\mathbf{r} = \{r_1, r_2, r_3\}$ .
- (ii) Apply a discrete grid-adaptive filter (GAF) to each field in order to introduce an appropriate backscatter length scale and level of anisotropy into the final acceleration field,  $\hat{\boldsymbol{\phi}} = \{\hat{\phi}_1, \hat{\phi}_2, \hat{\phi}_3\}$  - this procedure is described in Section 2.2.
- (iii) Scale each field to ensure the appropriate energy backscatter rate throughout the domain,  $\boldsymbol{\phi} = \{\phi_1, \phi_2, \phi_3\}$  - a new scaling procedure is described in Section 2.3.
- (iv) Take the curl of the three fields to produce a divergence-free (since  $\nabla \cdot (\nabla \times \boldsymbol{\phi}) = 0$ ) acceleration field,  $\mathbf{a} = \{a_1, a_2, a_3\}$ .

Each backscatter acceleration field lasts for a time period  $T_B$ , before a completely new (independent) field is generated. There are no gaps in-between each field, i.e. the backscatter accelerations are added to the LES field at every timestep within each  $T_B$  time period. The ensemble-average (denoted by an overbar) change in resolved kinetic energy due to the backscatter accelerations is well approximated by  $\Delta K = 1/2 \left( \overline{(u_i + a_i T_B)^2} - \overline{u_i^2} \right) = 1/2 \overline{a_i^2} T_B^2$  (sum over  $i$ ); the expanded terms involving  $\overline{u_i a_i}$  vanish since  $a_i$  has zero mean and is uncorrelated with  $u_i$ . Dividing through by  $T_B$  and noting that  $\overline{a_i^2}$  is simply the variance of  $a_i$ , we thus define a modelled energy backscatter rate,  $\hat{B}_r$ , as

$$\hat{B}_r = \frac{T_B}{2} (\sigma_{a_1}^2 + \sigma_{a_2}^2 + \sigma_{a_3}^2), \quad (2)$$

Mason and Brown (1994) demonstrated empirically that, despite having unrealistically high frequency, a value of  $T_B$  on the order of the model timestep,  $\Delta t$ , still gives significant reduction in excessive velocity shear, whilst also ensuring Galilean invariance. We use a theoretical energy backscatter rate,  $B_r$ , based on an estimation of fluctuating stress gradients within the LES fields (Mason and Thomson, 1992):

$$B_r = C_B \left( \frac{l}{l_0} \right)^5 \epsilon \quad (3)$$

where  $C_B$  is the backscatter coefficient, which typically takes a value within the range 0.6 – 1.4 (Weinbrecht and Mason, 2008, Chasnov, 1991, Mason and Thomson, 1992),  $\epsilon$  is the dissipation rate and  $l$  is the subgrid-scale mixing length in the Smagorinsky model, with maximum value  $l_0$  in well-resolved interior regions of the flow. Combining Eqs. (2) and (3), our aim is thus to scale each backscatter acceleration field such that

$$\sigma_{a_1}^2 + \sigma_{a_2}^2 + \sigma_{a_3}^2 = \frac{2C_B}{T_B} \left( \frac{l}{l_0} \right)^5 \epsilon. \quad (4)$$

We take  $l_0 = C_S \Delta$ , where  $C_S$  is the Smagorinsky coefficient and  $\Delta$  is the grid scale. For anisotropic grids, the ‘equivalent grid scale’ (Deardorff, 1970) is used, namely  $\Delta = \Delta_{eq} = (\Delta x \Delta y \Delta z)^{1/3}$ . For grids with vertical refinement only,  $\Delta_{eq}$  is assumed spatially uniform, with  $\Delta z$  taken as a typical value in the flow interior. For  $l$  we use the following equation to match the near-surface mixing length – which scales on  $\kappa(z + z_0)$ , where  $\kappa$  is the von-Kármán constant and  $z_0$  is the surface roughness – to the mixing length in well-resolved regions (Mason and Thomson, 1992):

$$l = \left( \frac{1}{l_0^n} + \frac{1}{(\kappa(z + z_0))^n} \right)^{-1/n} \quad (5)$$

where the exponent  $n$  controls how sharply the near-surface mixing length is matched to the value in the well-resolved flow interior.

## 2.2. Grid-adaptive filter (GAF)

This section outlines the new filtering procedure used in the generation of the backscatter acceleration fields, which allows the local backscatter length scale and anisotropy to be controlled independently of the model grid. The procedure utilises a discrete 3-D “grid-adaptive” filter that is applied directly on the model grid, thus removing the need for any interpolation from a secondary grid as with the WM08 model. We start by imposing that the 3-D filter is separable, i.e. that it can be constructed from a sequence of convolutions in the three lower dimensions (Wirjadi and Breuel, 2005):

$$h(x, y, z) = h_x(x) * h_y(y) * h_z(z) \quad (6)$$

where, e.g.,  $h_x(x)$  is the 1-D filter kernel in the  $x$ -dimension. The 3-D 1:2:1 filter is an example of a separable filter; the filtered field can be obtained by applying a 1-D filter with weights  $A \times [1 \ 2 \ 1]$  in the  $x$  then  $y$  then  $z$  dimension (the coefficient  $A$  determines the variance of the resulting field). However, rather than fixing the filter weights (and thus the number of grid points used in the calculation of each filtered value), we instead define a physical length scale (which may vary spatially) for each 1-D filter. The number of grid points used in the calculation of any filtered value is then dependent on the local grid spacing in each dimension.

To decide upon the shape of each 1-D filter, we may be guided by the choice of previous models. On an isotropic grid with resolution  $\Delta$ , it can be shown that the 3-point 1:2:1 filter (used in the MT92 model) and the 5-point 1:4:6:4:1 filter (used in the WM08 model) are both close approximations to the discrete Gaussian filter, with a filter width equal to  $0.8\Delta$  and  $\Delta$ , respectively. These choices of filter reflect the fact that the implicit filtering imposed by the

Smagorinsky model on the smallest resolved scales is Gaussian in nature (Sullivan *et al.*, 2003). We therefore also choose a Gaussian filter shape, which also facilitates comparison of our results with those obtained using the MT92 and WM08 models. Defining the filter width to be the standard deviation of the Gaussian function (Geurts, 2004), the continuous 1-D filter kernel for the general dimension  $\zeta$  is given by

$$h_\zeta(\xi) = A \exp\left(-\frac{\xi^2}{2(l_B^\zeta)^2}\right) \quad (7)$$

where  $\xi = \zeta - \zeta_f$  is the distance away from the filter centre at  $\zeta_f$ ,  $l_B^\zeta$  is the filter width for dimension  $\zeta$ , and the coefficient  $A$  controls the variance of the filtered field. For a discrete Gaussian filter, with which weights are only applied at a finite number of grid points, the weight at a grid point a distance  $\xi$  away from the filter centre-point,  $W_\xi$ , may be calculated as the integral over the part of the Gaussian function for which that grid point is closest (between  $\xi_-$  and  $\xi_+$ , say), i.e.:

$$W_\xi = A \int_{\xi_-}^{\xi_+} h_\zeta(\xi) d\xi = A l_B^\zeta \sqrt{\frac{\pi}{2}} \left\{ \operatorname{erf}\left(\frac{\xi_+}{l_B^\zeta \sqrt{2}}\right) - \operatorname{erf}\left(\frac{\xi_-}{l_B^\zeta \sqrt{2}}\right) \right\} \quad (8)$$

where  $\operatorname{erf}$  is the error function, which must be approximated numerically. For a grid with variable grid spacing, we take  $\xi_- = \xi - \Delta_-/2$  and  $\xi_+ = \xi + \Delta_+/2$ , where  $\Delta_-$  and  $\Delta_+$  are the distances between the given grid point and the adjacent grid points in the negative and positive  $\zeta$  direction, respectively. For computational efficiency, we restrict the number of grid points at which the filter weights are calculated to those for which  $|\xi| \leq 3l_B^\zeta$ , which ensures that at least 95 % of the area under the Gaussian function is accounted for.

For most applications, the coefficient  $A$  is chosen to normalise the filter (i.e. make its full integral equal to 1), which ensures that a constant region of an unfiltered flow-field is

unchanged after filtering. This is not important here, since there is no useful information contained within the initial random fields, and we may instead choose  $A$  to control the variance of the filtered fields. At this stage, we choose to maintain unit variance everywhere, and will apply an appropriate re-scaling of the fields at a later step (see Section 2.3). Given that the unfiltered fields are a random sample of values from the uniform distribution with zero mean and unit variance, then in order to maintain unit variance after filtering, we require

$$A = \left( \sum_{\xi} w_{\xi}^2 \right)^{-\frac{1}{2}} \quad (9)$$

where  $w_{\xi} = W_{\xi}/A$ .

We must now decide upon the width of each 1-D filter. This should be guided by the expected local backscatter length scale,  $l_B$ . As we are modelling backscatter from the unresolved scales, we aim to scale the backscatter length scale on the LES filter width,  $l_f$ , in well-resolved regions. However, the Smagorinsky SGS model assumes an implicit LES filter, and defining  $l_f$  is not trivial. It is commonly assumed that the filter width scales with the grid mesh size, i.e.  $l_f \sim \Delta_{eq}$ , where again,  $\Delta_{eq} = (\Delta x \Delta y \Delta z)^{1/3}$  is an estimate of the effective grid resolution (Deardorff, 1970), with  $\Delta z$  is taken as a typical value in the flow interior for vertically stretched grids. To allow a degree of flexibility, we define the backscatter length scale in well-resolved regions as  $l_B = \lambda (\Delta x \Delta y \Delta z)^{1/3}$ , where the parameter  $\lambda$  can be used to fine-tune  $l_B$ , but should be of order of unity. Closer to the surface, the local turbulence production scale eventually reduces below the LES filter width; in this region, we assume that the backscatter length scale decreases with the ratio of the local subgrid mixing length,  $l$ , to the subgrid mixing length in well-resolved regions,  $l_0$ . Thus, the backscatter length scale is fully defined as

$$l_B = \frac{l}{l_0} \lambda (\Delta x \Delta y \Delta z)^{1/3}, \quad \lambda = \mathcal{O}(1), \quad (10)$$

We further note that the local level of anisotropy in the backscatter acceleration fields can be controlled through the local ratio between the three backscatter length scale components:  $l_B^x$ ,  $l_B^y$ , and  $l_B^z$ . To ensure the overall backscatter length scale remains at  $l_B$ , we enforce the following constraint everywhere:

$$(l_B^x l_B^y l_B^z)^{1/3} = l_B. \quad (11)$$

The physical anisotropy of accelerations at the subgrid scale may be estimated from coarse-grained higher-resolution LES / lower-Reynolds-number direct numerical simulation (DNS). We may also attempt to infer the acceleration variances from (more readily available) velocity variance data. To do this, we first use  $\epsilon = C_\epsilon E^{3/2}/l$ , where  $C_\epsilon$  is a constant and  $E$  is the turbulent kinetic energy, as an estimate for the dissipation rate in Eq. (4) to obtain  $\sigma_{a_1}^2 + \sigma_{a_2}^2 + \sigma_{a_3}^2 = 2C_B C_\epsilon l^4 E^{3/2}/T_B l_0$ . Since  $E = 1/2 (\sigma_u^2 + \sigma_v^2 + \sigma_w^2)$ , then in isotropic turbulence, we have that the backscatter acceleration fluctuations and the velocity fluctuations are related by  $\sigma_a^2 \propto \sigma_u^3$ . We then make the assumption that in anisotropic turbulence, this relationship also holds for the individual components, and thus that the acceleration variance ratios are related to the velocity variance ratios by:

$$\frac{\sigma_{a_i}^2}{\sigma_{a_j}^2} = \frac{\sigma_{u_i}^3}{\sigma_{u_j}^3} \quad (12)$$

With the assumed local ratios of acceleration variance,  $\sigma_{a_1}^2 : \sigma_{a_2}^2 : \sigma_{a_3}^2$ , in place, it is possible to calculate the local values of  $l_B^x$ ,  $l_B^y$ , and  $l_B^z$  for the 1-D filters (see APPENDIX A1).

The use of the discrete grid-adaptive Gaussian filter is demonstrated in Figure 2, for the example case of  $l_B = 0.8\Delta x$  (at all heights) and  $\sigma_{a_1}^2 : \sigma_{a_2}^2 : \sigma_{a_3}^2 = 1:1:1$  everywhere (i.e. fully

isotropic backscatter). Figure 2(a) shows the filter weights in the  $z$ -dimension when the filter is centred on a grid point at  $z = z_f$ , on a grid with a fixed horizontal-to-vertical grid aspect ratio, for four separate grids with  $\alpha = \Delta x / \Delta z = 1, 2, 4$  and  $8$  respectively. Figure 2(b) shows the filter weights in the  $z$ -dimension when the filter is centred on three separate grid points on a stretched vertical grid; it can be seen that the filter width remains fixed, whilst the number and size of the filter weights adapt accordingly to ensure that the variance of the filtered fields remains unity everywhere.

### 2.3. New scaling procedure

When modelling horizontally homogeneous flow with a vertically refined grid only, then, of two variables ( $l$  and  $\epsilon$ ) on the right hand side of Eq. (4),  $l$  varies only with height, and gradients in  $\epsilon$  are much greater in the vertical than in the horizontal. Thus, when scaling the backscatter acceleration fields, it seems reasonable to apply a scaling factor that varies only in the vertical, and ensures that the variance on any horizontal grid level, with index  $k$ , is equal to

$$(\sigma_{a_1}^2 + \sigma_{a_2}^2 + \sigma_{a_3}^2)_k = \frac{2C_B}{T_B} \left( \frac{l_k}{l_0} \right)^5 \langle \epsilon \rangle_k, \quad (13)$$

where the subscript  $k$  denotes a quantity at grid level  $k$ , and angled brackets denote a horizontal average. The MT92 and WM08 models both employ a point-wise scaling factor rather than one based on a horizontally averaged dissipation rate. However we have tested both types of scaling factor (not shown) and found they give very little difference in output flow statistics. This was also found to be the case in the simulations performed by Mason and Brown (1994). We therefore choose the simpler vertical scaling factor option, as not only does it save on computational cost, but it also allows for analytical solutions to Eq. (13).



We denote  $g_k$  as the vertical scaling factor at grid level  $k$ . In APPENDIX B1 we show that each  $g_k$  is the solution of a quadratic equation (Eq. (22)), involving the theoretical backscatter rate as well as terms that depend on the local grid spacing and filtering procedure used. We have found that the discriminant,  $b^2 - 4ac$ , of this quadratic equation can become negative near the surface, where the theoretical energy backscatter rate falls sharply to zero, indicating that no real solutions exist for  $g_k$ . When this happens, we set the discriminant to zero to allow a real value of  $g_k$  to be calculated. This modifies the imposed backscatter rate away from the intended theoretical value. To correct this, we must apply another scaling factor at these grid levels after the curl operation, which is calculated empirically. This ‘post-curl’ scaling factor has the unwanted effect of reintroducing divergences into the backscatter acceleration field at these grid levels. Although these divergences are immediately removed by the pressure solver, this action results in a small but unwanted reduction in the backscattered energy (Weinbrecht and Mason, 2008). Fortunately, our testing shows (see Section 4.1) that this only affects a very small region close to the surface;  $z/H \lesssim 0.01$ , where  $H$  is the boundary layer scaling height.

When employing a grid with horizontal and vertical grid refinement, it is necessary to use a point-wise scaling factor. A point-wise scaling is also necessary when the turbulent flow-field is not horizontally homogeneous, since the use of a horizontally averaged dissipation rate,  $\langle \epsilon \rangle_k$ , is no longer appropriate in this case. We denote  $g_{i,j,k}$  as the point-wise scaling factor at the grid point with discrete indices  $i, j, k$  in the  $x, y, z$  direction, respectively. In this case, an equation for  $g_{i,j,k}$  (see APPENDIX B2) follows from the assumption that local gradients in the point-wise scaling factor are small. In reality, non-zero local gradients cause deviations away from the intended point-wise backscatter rates in the curled field. As with the vertical scaling factor procedure, the biggest problems occur very near the surface where the theoretical backscatter rate drops rapidly. To help correct this, an empirically calculated

vertical scaling factor again is applied after the curl operation to ensure that Eq. (13) is satisfied at each grid level, i.e. that the horizontally averaged backscatter rate is at-least always recovered. The resulting divergences introduced into the acceleration field are typically comparable in size to those seen with the vertical scaling factor procedure for the same case.

### 3. Large-eddy simulation configuration

This paper focuses on the methodology of the new backscatter model; in particular, the new grid-adaptive filter (GAF) described in Section 2.2. However, we also aim to validate the GAF model for the case of LES of the neutral ABL over flat, homogeneous terrain. This allows us to compare the results obtained with the GAF model against those obtained with the MT92 and WM08 models, since such a case can be sufficiently modelled using a grid with vertical stretching only and thus all three backscatter models remain applicable. The wider applicability of the GAF model to more complex cases involving local 3-D grid refinement is left for future work.

Colorado State University's Regional Atmospheric Modelling System (RAMS) is used in the present study. Further details of the model specification can be found in Cai (1999). The Smagorinsky SGS model is used, with coefficient  $C_S = 0.15$ . The specified initial profiles are for a neutral boundary layer, with a constant potential temperature of 300 K throughout the entire depth of the domain, and a wind profile based on the Ekman spiral at latitude  $45^\circ$  with a geostrophic wind speed of  $U_g = 5 \text{ m s}^{-1}$ . Other selected parameters include a von-Kármán constant of  $\kappa = 0.35$ , following the analysis by Businger *et al.* (1971) of the ABL observations carried out in Kansas in 1968, a surface roughness of  $z_0 = 0.1 \text{ m}$  and a model timestep of  $\Delta t = 0.3 \text{ s}$ . A Monin-Obukhov boundary condition is applied at the first grid level above the surface (at  $z = z_1$ ) which, for the neutral case, enforces a horizontal wind

speed of  $U(z_1)/u_* = (1/\kappa) \ln(z_1/z_0)$ , where  $u_*$  is the friction velocity. This is common practice in rough-wall geophysical flows, including in studies that (like the current one) also test the ability of LES to reproduce Monin-Obukhov similarity theory above the first grid level (e.g., Lu and Porté-Agel (2014), Kirkil *et al.* (2012), Sullivan *et al.* (1994)). However, as Sullivan *et al.* (1994) points out, we note that this approach is only justified if the grid mesh is refined enough that at least part of the surface layer is explicitly resolved by the LES model. The depth of the neutral boundary layer scales with  $u_*/|f|$ , where  $f$  is the Coriolis parameter (Garratt, 1994). In our simulations,  $u_* = 0.2$  is a typical value for  $u_*$  and  $f = 1.0 \times 10^{-4}$ ; we thus define a scaling height of  $H = 2000$  m, which we use to scale  $z$  in plots.

The performance of the backscatter model should not be significantly affected by the chosen grid aspect ratio. Large aspect ratios are common in LES studies of the ABL, often in order to match the physical anisotropy of surface layer turbulence with the anisotropy of the near-surface grid. Typical grid aspect ratios tested for LES studies of the neutral ABL fall within the range  $\alpha = \Delta x/\Delta z = 1$  to 10 (Mirocha *et al.*, 2012, Chow *et al.*, 2005, Sullivan *et al.*, 1994). Thus here we test the backscatter models on four different model grids that cover this range. We use  $64 \times 64$  grid points in the  $x$ - and  $y$ - directions with  $\Delta x = \Delta y = 50$  m. For the vertical grid, we define  $\Delta z_1$  as the height of the lowest grid point above the surface, and apply a constant vertical grid stretch factor,  $S_{\Delta z} = 1.03$ , such that  $\Delta z_{k+1} = S_{\Delta z} \times \Delta z_k$ , until  $\Delta z = \Delta z_{\max} = 50$  m, after which  $\Delta z$  remains fixed at  $\Delta z_{\max}$  up to the top of the domain, at around 2500 m in all cases. This is summarised in Table I.

LES output obtained with the new stochastic backscatter model (GAF) are compared against results obtained using the Smagorinsky model alone (SMAG), as well as the MT92 and WM08 models, which have also been implemented into the LES code. To allow a direct comparison of the results obtained with each backscatter model, the following model

parameters are set constant over each model, and are potentially different from those used in the original papers for the MT92 and WM08 models. For the GAF model, we use  $\lambda = 1$  in Eq. (10), which defines a discrete Gaussian filter that is well approximated by the 1:4:6:4:1 filter on an isotropic grid; we thus use the 3-D 1:4:6:4:1 filter for both the MT92 and WM08 models. We take  $n = 4$  for the mixing length exponent in Eq. (5). The backscatter coefficient is set to  $C_B = 0.6$ . A new backscatter acceleration field is generated every other model timestep, thus we take the time scale of the backscatter acceleration fields to be  $T_B = 2\Delta t$ . Finally, as the influence of backscatter is minimal far enough above the near-surface region, computational expense can be spared by defining a maximum height,  $z_{B_{\max}}$ , below which the backscatter accelerations are added to the LES field. Here we take  $z_{B_{\max}} = 500$  m, which corresponds to a height of around  $0.2H$ . This is summarised in Table II.

With the GAF model, we attempt to relate the backscatter anisotropy to the physical anisotropy of the subgrid scales by using measured velocity variance data. We use the velocity variance profiles reported by Grant (1986) (his Figure 5) in near-neutral conditions. We note that the reported variances encompass a wide range of turbulence length scales, and it must be assumed that the variance ratios are characteristic of the variance ratios at the subgrid scales. We simplify the data somewhat by taking the two horizontal variance components to be equal (to be consistent with the MT92 and WM08 models for the sake of later comparison) and fit a smooth exponential curve roughly through the data points, such that the velocity variance ratios at the surface are taken as  $\sigma_u^2 : \sigma_v^2 : \sigma_w^2 = 4 : 4 : 1$ , and are essentially isotropic above  $0.2H$ . Using Eq. (12), the imposed backscatter acceleration variance ratios are thus taken as  $\sigma_{a_1}^2 : \sigma_{a_2}^2 : \sigma_{a_3}^2 = 8 : 8 : 1$  at the surface – the full variance ratio profiles are plotted in Figure 3(a). We emphasise that these ratios might be considered as an example, used to demonstrate the GAF model, and that any other ratios (that allow for

realizable solutions of  $l_B^\zeta$ ) could be applied. Figure 3(b) shows the resulting profiles (on grid G4) of the normalised backscatter length scale components,  $l_B^\zeta/\hat{l}_B$ , where  $\hat{l}_B$  is the backscatter length scale in the isotropic flow interior. This plot also shows how the backscatter length scale decreases close to the surface with the GAF model, in line with the subgrid mixing length scale.

## 4. Results and discussion

We first analyse the characteristics of the backscatter acceleration fields in isolation (Section 4.1) and then look at their effects on the LES fields (Section 4.2). Finally, we assess the additional CPU time required by the backscatter model and compare this to simply increasing the grid resolution with the Smagorinsky model (Section 4.3).

### 4.1. Backscatter acceleration fields

Figure 4 shows surface layer contour plots through three example backscatter acceleration fields, generated using (a) the MT92 model, (b) the WM08 model, and (c) the GAF model, respectively, on grid G4 (which has a near-surface grid aspect ratio of  $\Delta x/\Delta z \approx 10$ ). Each plot shows point-wise acceleration magnitudes, i.e.  $a = \sqrt{a_1^2 + a_2^2 + a_3^2}$ , normalised by the maximum value within that field. The dissipation field used to calculate the local backscatter rate was taken from a quasi-steady LES, without backscatter, on the same grid. It can be seen that the backscatter is most significant within the lower part of the surface layer. With all three models, the characteristic length scale of individual backscatter structures away from the surface scales reasonably with the horizontal grid spacing, and thus with the scale of the LES filter width. Nearer the surface, the backscatter length scale can just be seen to begin to decrease with the GAF model in line with the subgrid mixing length scale, though this is hidden very close to the surface by the small acceleration magnitudes there. With the MT92 model, the backscatter anisotropy can be seen to depend on the local vertical grid spacing.

Consequently, the field is excessively anisotropic on the highly refined near-surface grid. With the WM08 model, the backscatter looks to remain locally isotropic (with individual structures as tall as they are wide) at all grid levels, as expected from the interpolation method used to generate the acceleration fields. There are apparent discontinuities in the field at some grid levels, where individual backscatter structures seem to be slightly misaligned. However, this doesn't appear to affect the time-averaged LES statistics at these levels (shown later). The anisotropy within the backscatter acceleration field generated using the GAF model falls somewhere in-between the MT92 and WM08 models; it is neither fixed to the vertical grid spacing, nor spatially uniform, but looks to follow the imposed profile shown in Figure 3(a), with modest anisotropy close to the surface, becoming gradually more isotropic with distance from the surface. This is more formally verified next.

The spatial anisotropy within the backscatter acceleration fields described above is quantified in Figure 5, which shows, for each model, normalised surface-layer profiles of the three variance components,  $\sigma_{a_1}^2$ ,  $\sigma_{a_2}^2$  and  $\sigma_{a_3}^2$ , and their sum, which should equate to the target backscatter variance profile as given by the right hand side of Eq. (13) (also plotted for comparison). The data are normalised by the maximum of the target profile. The plots show that the target profile of summed variance components is well met by all three backscatter models. With the MT92 model, however, the vertical variances are considerably smaller than the horizontal variances at all grid levels, as a result of the application of the 3-D 1:4:6:4:1 filter on the vertically refined grid. Taking  $\Delta x = \Delta y$  in Eq. (21), and assuming that  $\Delta g_k \ll g_k$  (and thus that  $g_{k+1} \approx g_k$ ), it follows that the ratio of the vertical variance to either of the horizontal variance components in MT92 the backscatter acceleration fields is

$$\frac{\sigma_{a_3}^2}{\sigma_{a_1}^2} = \frac{\sigma_{a_3}^2}{\sigma_{a_2}^2} = \frac{2}{1 + \alpha^2}, \quad (14)$$

where  $\alpha = \Delta x / \Delta z_k$  is the local horizontal-to-vertical grid aspect ratio. Setting  $\alpha = 10$  in Eq. (14), we can approximate the vertical variance component to be around 2 % of the horizontal variance components near the surface. Such large anisotropy in the acceleration fields is detrimental to the performance of the backscatter model (as shown in later results) since, from a pragmatic point of view at least, the inclusion of backscatter is intended to reduce the excessive velocity shear in the surface layer, which can only be achieved through an increased vertical mixing of momentum. When horizontal variances dominate, the mixing of momentum is only largely increased within horizontal planes, and thus the effectiveness of backscatter acceleration fields in smoothing out the velocity shear profile is reduced. With the WM08 model, the backscatter is largely isotropic at all grid levels as a result of linearly interpolating the accelerations from an isotropic grid, as can be understood by setting  $\alpha = 1$  in Eq. (14). With the GAF model, the observed backscatter anisotropy matches well with the imposed (target) anisotropy profile (shown by the dashed lines) at all grid levels. This confirms that the new filtering procedure is able to control spatial variations in the backscatter anisotropy, allowing for physical consistency with the anisotropy of the subgrid scales.

The backscatter model should also aim to generate acceleration fields that contain minimal divergences. A divergence-free backscatter acceleration field ensures that there are no force sources or sinks within any finite sub-volume of the domain. Conversely, any divergences in the backscatter acceleration fields may leave simulations prone to unphysical small-scale behaviour, and also lead to an unwanted reduction in the backscattered energy (Weinbrecht and Mason, 2008). The curl operation that is performed during the generation of the backscatter acceleration fields removes all divergences from the fields. However the application of the ‘post-curl’ vertical scaling factor, required at grid levels where real solutions to the ‘pre-curl’ scaling factor  $g_k$  (Eq. (22)) do not exist, reintroduces divergences

at those grid levels. Figure 6 summarises, for each backscatter model, the magnitude of the grid-cell divergences (calculated as  $(a_1^{i+1,j,k} - a_1^{i,j,k})/\Delta x + (a_2^{i,j+1,k} - a_2^{i,j,k})/\Delta y + (a_3^{i,j,k+1} - a_3^{i,j,k})/\Delta z_k$ ) within the surface layer, for the same three example backscatter acceleration fields described above (generated on grid G4). The plots show normalised root-mean-square (RMS) values at each grid level (equivalent to the standard deviations, since their mean is zero). The accelerations have been normalised by  $\sigma_a/\Delta_{\text{eq}}$ , where  $\sigma_a$  is the square root of maximum of the target backscatter variance profile (given by the right hand side of Eq. (13)) and  $\Delta_{\text{eq}}$  is 50 m in this case – this normalising factor scales with the magnitude of spatial variations of the largest backscatter accelerations. The plots show that real solutions of  $g_k$  exist throughout most of the surface layer, but the post-curl scaling factor is required at the lowest 4 or 5 grid levels (within the region  $z/H \lesssim 0.01$ ) in each case, introducing divergences there as a consequence. The largest divergences exist within the backscatter acceleration fields generated with the WM08 model. The divergences are around half the size with the GAF model, and considerably smaller with the MT92 model. The magnitude of the divergences corresponds to the level of anisotropy within the backscatter acceleration fields, and is related to the use of the curl operator in the region where the backscatter rate profile falls sharply to zero at the surface from its maximum at around  $0.2H$ ; as the operator involves differences between adjacent grid levels, it is easier to accommodate such a sharp vertical gradient as the autocorrelation between the two adjacent grid levels is reduced. With the GAF model, the magnitude of divergences within backscatter acceleration fields thus depends on the imposed level of anisotropy. As would be expected, the GAF model divergence profiles are almost identical to the MT92 and WM08 model profiles when the anisotropy level is set to match that of the respective model (not shown).



## 4.2. LES fields

We assess the performance of the GAF backscatter model, as well as the previous models, from the surface-layer profiles of mean nondimensional velocity shear, for the set of LES runs outlined in Section 3. The profiles are normalised such that the expected value is equal to 1 within the neutral surface layer, and follows from differentiation of the neutral logarithmic wind profile (Von Kármán, 1931) assuming zero displacement length (Lu and Porté-Agel, 2014):

$$\begin{aligned}
 U(z) &= \frac{u_*}{\kappa} \ln \left( \frac{z + z_0}{z_0} \right) \\
 \Rightarrow \Phi_M &= \frac{dU}{dz} \frac{\kappa(z + z_0)}{u_*} = 1
 \end{aligned} \tag{15}$$

in which  $u_*$  is the friction velocity. In 3-dimensional flow, we take  $dU/dz = \sqrt{(\partial u/\partial z)^2 + (\partial v/\partial z)^2}$ . Each profile is the result of a horizontal average over all grid points on a given grid level and over 3 hours of simulation time, after a quasi-steady state is adjudged to have been reached. The resulting profiles are shown in Figure 7.

The profiles show that the GAF model is able to significantly reduce the maximum of the ‘overshoot’ in  $\Phi_M$  (from that obtained without backscatter, i.e. with the Smagorinsky model alone) towards the expected value of 1. Importantly, this reduction appears to be largely independent of the level of vertical grid refinement, at least for the cases tested here, which span a grid aspect ratio range of  $\alpha = \Delta x/\Delta z = 1$  to 10. The  $\Phi_M$  maximum is reduced from 2.27 to 1.27 on grid G1, from 2.35 to 1.38 on grid G2, from 2.19 to 1.23 on grid G3, and from 2.11 to 1.21 on grid G4, thus giving a typical reduction of around 80%. The height of the  $\Phi_M$  maximum is also brought closer to the ground with the backscatter model, occurring at around 1/3 of the surface-layer depth without backscatter and around 1/6 of the surface-layer

depth with backscatter (though the vertical resolution is too coarse to confirm this for grid G1). The performance of the GAF model is fairly similar to that of the WM08 model; however there is a further improvement of around 5% with the GAF model in reducing maximum excessive  $\Phi_M$  on 3 of the 4 grids tested (G1, G3 and G4). Conversely, the reduction in the  $\Phi_M$  overshoot with the MT92 model is shown to depend heavily on the grid aspect ratio. On an isotropic grid (G1), the model is essentially as effective as the other two backscatter models; this is not surprising, since the MT92 backscatter acceleration fields are fully isotropic in this case. The model appears to remain effective for grids with modest anisotropy, i.e. on grid G2 with  $\alpha = 2$ . However, for larger aspect ratios (grids G3 and G4), the reduction in  $\Phi_M$  becomes less pronounced as the vertical grid refinement within the surface layer increases. This illustrates how an overly-large level of anisotropy within the backscatter acceleration fields can act to reduce the effectiveness of the backscatter model due to a reduction in the downward mixing of momentum from the upper part of the surface layer. Mirocha *et al.* (2010) found that the expected similarity solution for wind speed within the surface layer is best reproduced by the Smagorinsky model for grid aspect ratios of around  $\alpha = 4$ ; we thus reason that the range of grid anisotropies over which the MT92 model remains effective is too small.

There are two key reasons for the justification of the new GAF backscatter model, despite the relatively small difference in performance from the WM08 model for the simulations performed here:

- i. ***Improved physics*** – The GAF model is able to control the backscatter length-scale (eddy-size) and anisotropy (eddy-shape). This means that the inclusion of backscatter can be implemented in a manner that is more physically consistent with reality. One of the principles of backscatter theory dictates that the dominant backscatter length

scale from the unresolved (SGS) to the resolved scales should match the local grid-scale (Mason and Thomson, 1992). The GAF model follows this principle closely from the middle of the boundary layer down through the surface layer. The WM08 model, however, violates the principle in the surface layer, since the backscatter length-scale is fixed everywhere at the grid-scale of the flow interior. Thus, within the surface layer, where eddy sizes are smaller and turbulence structure is known to be anisotropic with smaller vertical than horizontal extent (Kaimal *et al.*, 1972), the vertical length-scale is unphysically large. From a spectral point of view, this corresponds to energy being added at inappropriately large wavelengths (or small wave-numbers). The WM08 model thus induces an unfairly high degree of vertical mixing, bringing higher momentum flow down towards the region of excessive velocity shear and smoothing out the overshoot there. It is therefore to the GAF model's credit that it performs at least as well as the WM08 model despite this – we offer reasons for why this might be the case in the next paragraph.

- ii. ***Wider applicability*** – The simulations performed in this paper (of a fully neutral ABL over homogeneous, flat terrain) require LES grids with vertical stretching only, thus allowing us to test and compare both models (GAF and WM08), which are both applicable on such grids. However, the WM08 model is not applicable in more complex modelling cases in which local 3-D grid refinement is utilised, since the backscatter length-scale is fixed and so cannot be varied spatially to account for local changes in the LES filter width, whereas the GAF model is capable of doing this.

One might have expected a monotonic relationship between the reduction in maximum  $\Phi_M$  and the level of anisotropy within the backscatter acceleration fields, on the presumption that larger anisotropy (with smaller vertical variances than horizontal) results in less vertical mixing of momentum and thus a larger maintained velocity gradient within the surface layer.

However, the results obtained with the GAF model e.g. on grids G3 and G4 show that this is not the case. We propose two possible reasons for this. Firstly, we note that with increasing anisotropy in the backscatter acceleration fields, there are smaller near-surface divergences which will thus result in smaller associated losses of the backscattered energy, and this may initially outweigh the reduction in performance associated with reduced vertical mixing. Secondly, it is hoped that when the backscatter length scale and anisotropy are more closely matched to grid-scale turbulence length scale and anisotropy within the LES flow-field, the backscatter accelerations will be more readily ‘taken up’ by the grid-scale flow structures, and consequently more effective in reducing the  $\Phi_M$  overshoot. Either way, the results demonstrate that by controlling the spatial structure of the backscatter acceleration fields, the GAF model is, in some cases, able to further reduce excessive  $\Phi_M$  over that which is possible with fully isotropic backscatter.

It is encouraging to note the similarity between the WM08 and MT92 profiles in Figure 7(c) and the equivalent profiles in the Weinbrecht and Mason (2008) paper (their Figure 1, left), which were plotted from runs on a similar model grid and in neutral conditions. Although the maximum absolute value of  $\Phi_M$  within the surface layer is slightly larger in our simulations than in theirs, this is also true for the profiles without backscatter (i.e. with the Smagorinsky model alone), and the percentage reduction in excessive  $\Phi_M$  remains similar. We therefore reason that the absolute differences are simply a result of the different LES codes used in each study. We also note that it is possible to reduce the excessive velocity shear within the lower part of the surface layer further towards 1 by increasing either the backscatter coefficient,  $C_B$ , or the filter width (i.e. increasing  $\lambda$  in the GAF model). However, we have found that this can often lead to an over-reduction in  $\Phi_M$  (i.e. values below 1) in the upper part of the surface layer (not shown for brevity). We have not attempted to find the optimal ‘tuning’ of the model parameters in this study, since we are mainly interested in comparing

the relative performance of the GAF model against the previous models for any given set of reasonable parameters.

The backscatter acceleration fields constitute a continuous modification to the LES fields which, it is argued, bring the model closer towards reality. Similarly, should the backscatter acceleration fields be abruptly removed, we would expect the model to tend back towards its original state, further from reality. There should therefore exist a time scale over which this change occurs, which we interpret as a physical time scale associated with the effects of backscatter at the grid-scale. We attempt to objectify this time scale in the following way. We start from a quasi-steady simulation without backscatter; here we use the run performed on grid G3. We then turn on each backscatter model in turn and observe the subsequent changes to the LES fields. Specifically, we track the value of the maximum nondimensional velocity shear within the surface layer,  $(\Phi_M)_{\max}(t)$ , or  $S(t)$  for short, and plot the resulting time series. This is shown in Figure 8, along with a fitted exponential trend-line for each model (as described below). The raw time series have been smoothed with a 5-minute moving average filter to remove small (high frequency) fluctuations for the benefit of plotting. The relative success of a particular backscatter model can again be assessed by examining its ability to bring the maximum nondimensional velocity shear towards the expected value of 1.

The time series suggest the existence of a ‘backscatter adjustment time scale’ that is largely independent of the chosen backscatter model. We attempt to fit an exponential trend-line to each of the time series of the general form:

$$S(t) = (S_0 - S_\infty)e^{-t/\tau} + S_\infty \quad (16)$$

where  $S_0$  is the initial value of  $S$ , and  $S_\infty$  is the final quasi-steady value of  $S$ , which we take to be the mean value of  $S$  over the last third of the simulation period. It is found that a good fit can be obtained for all models with an e-folding time of  $\tau \approx 10$ -15 minutes. This backscatter

adjustment time scale is comparable with the turnover time scale of surface-layer eddies, which is of order  $\Delta_{\text{SL}} / \sigma_{U,\text{SL}} \approx 200/0.3 \approx 11$  minutes, where  $\Delta_{\text{SL}}$  is the depth of the surface layer and  $\sigma_{U,\text{SL}}$  is a typical value for the square root of velocity variance within the surface layer (which we have approximated from Figure 9). This suggests that the largest surface-layer eddies are the most important mechanism through which the imposed backscatter accelerations eventually redistribute momentum, and thus reduce velocity shear, within the surface layer.

Figure 9 shows near-surface profiles of resolved velocity variance for the LES runs on model grid G4, obtained with the Smagorinsky model and each of the backscatter models. On their own, the backscatter acceleration fields provide a direct (positive) source of velocity variance to all three components. However, we observe that in all cases, the overall effect of backscatter is to redistribute the velocity variance among the three components so as to increase near-surface isotropy of the flow-field. This is seen as a reduction of the streamwise component and an increase in the crosswind and vertical components. The backscatter acceleration fields provide the means by which momentum from the upper part of the surface layer is mixed down towards the lower part, thereby reducing the excessive velocity shear observed when backscatter is not modelled. These results agree closely with Mason and Thomson (1992) who observed a similar redistribution among the three components of velocity variance, bringing them closer to the ratios observed in the upper surface layer by Grant (1986) in near-neutral conditions.

#### 4.3. Additional CPU time

Finally, we report on the additional CPU time required by the GAF backscatter model, over equivalent simulations without backscatter, i.e. with the Smagorinsky model alone. For a given simulation, this will vary with the backscatter model parameters selected, in particular

the height below which the backscatter accelerations are added to the LES fields,  $z_{B_{\max}}$ , the filter width parameter  $\lambda$  (and the number of standard deviations away from the filter centre point used for the discrete Gaussian filter kernel), and the time between each newly generated backscatter acceleration field,  $T_B$ . However, as an example, assessing the LES runs performed here on grid G3, the simulation with the GAF model required approximately 50% additional CPU time than the simulation with the Smagorinsky model alone. Although this could be considered a fairly large computational cost, we are able to get a better indication of the relative benefit of the backscatter model if we compare the surface-layer profile of mean nondimensional velocity shear  $\Phi_M$  obtained with the backscatter model on grid G3 against the profile obtained with the Smagorinsky model when the grid resolution is increased such that an additional 50% CPU time is required (for the same simulation time period). To this end, we tried a simulation in which the horizontal grid resolution was increased from  $\Delta x = \Delta y = 50$  m to around 40 m and  $\Delta z_{\max}$  was reduced to 40 m (whilst the domain extent was kept roughly the same in each dimension), and the model timestep was reduced accordingly from  $\Delta t = 0.3$  s to  $\Delta t = 0.25$  s. In fact, this simulation required almost twice as long (94% extra CPU time) to complete than with the original grid. Despite this, the results are still clear – increasing the grid resolution with the Smagorinsky model *does not* remedy the problem of erroneous velocity shear within the surface layer; it simply acts to shift the velocity shear profile maximum towards the surface (compare the solid grey and black lines in Figure 7(c)). This result has also been observed in previous studies (Chow *et al.*, 2005, Mason and Thomson, 1992). We may thus conclude that the backscatter model adds significant worth to the simulation for its computational cost that cannot be achieved by an increase in grid resolution with the Smagorinsky model alone. An additional advantage is that the imposed backscatter accelerations act to induce fully developed turbulence much faster than with the Smagorinsky model alone; thus a statistically steady state was achieved

significantly more quickly with the backscatter model (typically around 5 hours) than with the Smagorinsky model alone (typically around 10 hours) in our simulations. This again corroborates with previous work (Weinbrecht and Mason, 2008).

## 5. Conclusions

In this paper, a new method has been proposed for the generation of stochastic backscatter acceleration fields designed to impose fluctuations in the Smagorinsky subgrid stresses in large-eddy simulation modelling. The method employs a discrete “grid-adaptive” filter (GAF) that allows control of spatial variations in the backscatter length scale and anisotropy. Thus, unlike the previous models of Mason and Thomson (1992) and Weinbrecht and Mason (2008), with which these properties are either tied to the model grid or spatially uniform, the backscatter length scale can be appropriately reduced towards surfaces, and the backscatter anisotropy can be chosen to be consistent with the physical anisotropy of the subgrid scales. The backscatter length scale may also be varied in accordance with any spatial variations in the LES filter width, thus widening the applicability of the GAF model to studies of more complex flow geometries that utilise local 3-D grid refinement.

The GAF backscatter model was tested for the case of LES of the neutral ABL over flat, homogeneous terrain, for various levels of vertical grid refinement, and its performance analysed, along with the MT92 and WM08 models, in terms of its ability to reduce excessive nondimensional velocity shear within the surface layer (as seen with the Smagorinsky model alone) towards the expected value of 1. The GAF model was shown to significantly reduce the velocity shear ‘overshoot’ maximum by an amount that is largely independent of the near-surface grid aspect ratio, and typically around 80%. Conversely, the effectiveness of the MT92 model was shown to depend heavily on the level of grid refinement, with significant



reduction in model performance as the vertical resolution is increased, due to an associated reduction in the vertical mixing of momentum within the surface layer.

The level of divergences within the backscatter acceleration fields generated by the new and existing backscatter models was also analysed. Divergences leave simulations prone to unphysical small-scale behaviour and lead to an unwanted reduction in the backscattered energy, and should therefore be minimised. Divergences are reintroduced into the initially divergence-free acceleration fields at grid levels very close to the surface ( $z/H \lesssim 0.01$ ) where the application of a ‘post-curl’ scaling is required in order to ensure the correct horizontally-averaged energy input. The magnitude of these divergences was shown to correspond to the level of anisotropy within the backscatter acceleration fields; thus the smallest divergences were seen with the MT92 model (most anisotropic) and the largest with the WM08 model (fully isotropic), with the GAF model divergences falling somewhere in-between depending on the imposed level of backscatter anisotropy.

A backscatter adjustment time scale, corresponding to the e-folding time for the rate of reduction in excessive velocity shear within the surface layer, was also identified and found to be of order 10-15 minutes for all the backscatter models tested. This is also the time scale associated with the turnover time of the largest surface-layer eddies, indicating their importance as a mechanism through which the imposed backscatter accelerations can redistribute momentum, and thus reduce velocity shear, within the surface layer.

Future work shall initially focus on exploiting the wider applicability of the GAF backscatter model to more complex cases utilising local 3-D grid refinement, due to its ability to control the structure of the backscatter acceleration fields in accordance with spatial variations in the LES filter width. The application of the GAF model to a simulation of street canyon flow is

currently being carried out, with preliminary results indicating that the model leads to an improved representation of the primary vortex strength within the canyon.

The model could also be further improved by enforcing a more physically appropriate time scale for the backscatter accelerations, rather than one based on the model timestep, in the hope that this will bring further reduction in the excessive mean velocity shear within the surface layer. With appropriate modification to the theoretical backscatter rate, the model might also be applied in non-neutral stability regimes, and at other spatial scales.

### Acknowledgements

We are grateful to the UK Natural Environment Research Council and the UK Environment Agency for their financial support of this research. The computations described herein were performed using the University of Birmingham's BlueBEAR HPC service (<http://www.bear.bham.ac.uk>). We would also like to thank the referees and Professor Rob MacKenzie for their helpful comments.

## APPENDIX A

### *Calculation of the backscatter length scale components, $l_B^x$ , $l_B^y$ , and $l_B^z$*

To calculate the local values of  $l_B^x$ ,  $l_B^y$ , and  $l_B^z$  from the assumed local ratios of acceleration variance,  $\sigma_{a_1}^2 : \sigma_{a_2}^2 : \sigma_{a_3}^2$ , we use Eqs. (21) (for a vertically refined grid and horizontally homogeneous turbulence), with the assumption that  $\Delta g_k \ll g_k$  (and thus that  $g_{k+1} \approx g_k$ ), to obtain a set of three simultaneous equations (one for each of  $\sigma_{a_1}^2 / \sigma_{a_2}^2$ ,  $\sigma_{a_1}^2 / \sigma_{a_3}^2$  and  $\sigma_{a_2}^2 / \sigma_{a_3}^2$ ) at each grid level,  $k$ , with three unknowns; namely,  $\rho_k^{\Delta x}$ ,  $\rho_k^{\Delta y}$  and  $\rho_k^{\Delta z}$ . For horizontally inhomogeneous turbulence and/or for grids with vertical and horizontal refinement, we instead use Eqs. (23) to obtain a set of three equations at each grid point (note that as long as

the turbulence field is stationary, these equations need only be solved once, at the beginning of the simulation, reducing computational cost dramatically). Now, it can be shown that the spatial autocorrelation induced by the application of a continuous 1-D Gaussian filter (Eq. (7)) on a continuous 1-D white-noise field in the general dimension  $\zeta$  is

$$\rho^{\Delta\zeta} = \exp \left\{ - \left( \frac{\Delta\zeta}{2l_B^\zeta} \right)^2 \right\}. \quad (17)$$

We may thus use this equation, along with the constraint imposed by Eq. (11), to solve each set of simultaneous equations for  $l_B^x$ ,  $l_B^y$  and  $l_B^z$ . We achieve this using the following iterative procedure, which is found to give sufficiently accurate solutions after only one or two iterations: (i) select a sensible initial guess for  $l_B^x$ , e.g.  $l_B^x = l_B$ , and solve Eq. (17) for  $\rho^{\Delta x}$ ; (ii) use this result to solve Eq. (18) for  $\rho^{\Delta y}$ , which follows from elimination of  $\rho^{\Delta z}$  from the simultaneous equation set, and subsequently obtain  $l_B^y$  using Eq. (17); (iii) use this result to solve any one of the simultaneous equation set for  $\rho^{\Delta z}$ , e.g., Eq. (19), and subsequently obtain  $l_B^z$  using Eq. (17); (iv) multiply each of  $l_B^x$ ,  $l_B^y$  and  $l_B^z$  by the factor  $l_B / (l_B^x l_B^y l_B^z)$  to ensure that Eq. (11) is satisfied; (v) use the newly calculated value of  $l_B^x$  as the initial guess in the iteration process and repeat steps (ii) to (v) until a sufficient level of accuracy has been reached.

$$\rho^{\Delta y} = 1 - \frac{\Delta y^2 (1 - \rho^{\Delta x}) \left\{ \frac{\sigma_{a_1}^2}{\sigma_{a_3}^2} \left( 1 - \frac{\sigma_{a_1}^2}{\sigma_{a_2}^2} \right) - \frac{\sigma_{a_1}^2}{\sigma_{a_2}^2} \right\}}{\Delta x^2 \left\{ \left( 1 - \frac{\sigma_{a_1}^2}{\sigma_{a_3}^2} \right) \left( 1 - \frac{\sigma_{a_1}^2}{\sigma_{a_2}^2} \right) - 1 \right\}}, \quad (18)$$

$$\rho^{\Delta z_k} = 1 - \frac{\sigma_{a_1}^2}{\sigma_{a_2}^2} \frac{\Delta z_k^2 (1 - \rho^{\Delta x})}{\Delta x^2 \left( 1 - \frac{\sigma_{a_1}^2}{\sigma_{a_2}^2} \right)} + \frac{\Delta z_k^2 (1 - \rho^{\Delta y})}{\Delta y^2 \left( 1 - \frac{\sigma_{a_1}^2}{\sigma_{a_2}^2} \right)}. \quad (19)$$

Note that for real solutions of  $l_B^{\zeta}$  to exist with Eq. (17), we require  $0 < \rho^{\Delta\zeta} < 1$ , which is also a requirement on account of  $\rho^{\Delta\zeta}$  being a (positive) correlation coefficient. We have found that this requirement is met as long as the local grid aspect ratios do not differ significantly from the intended local ratios of the acceleration variance components.

## APPENDIX B

### *Scaling factor derivations*

#### B1. Derivation of the vertical scaling factor, $g_k$

For the vertical scaling factor, we have that  $\boldsymbol{\phi}^{i,j,k} = g_k \hat{\boldsymbol{\phi}}^{i,j,k}$ , where superscripts  $i, j$  and  $k$  also denote discrete grid-point indices. Choosing the forward-differencing discrete curl operator, the point-wise backscatter accelerations will be equal to

$$\mathbf{a}^{i,j,k} = \nabla \times \boldsymbol{\phi}^{i,j,k} = \begin{bmatrix} g_k(\hat{\phi}_3^{i,j+1,k} - \hat{\phi}_3^{i,j,k})/\Delta y - (g_{k+1}\hat{\phi}_2^{i,j,k+1} - g_k\hat{\phi}_2^{i,j,k})/\Delta z_k \\ (g_{k+1}\hat{\phi}_1^{i,j,k+1} - g_k\hat{\phi}_1^{i,j,k})/\Delta z_k - g_k(\hat{\phi}_3^{i+1,j,k} - \hat{\phi}_3^{i,j,k})/\Delta x \\ g_k(\hat{\phi}_2^{i+1,j,k} - \hat{\phi}_2^{i,j,k})/\Delta x - g_k(\hat{\phi}_1^{i,j+1,k} - \hat{\phi}_1^{i,j,k})/\Delta y \end{bmatrix} \begin{Bmatrix} i \\ j \\ k \end{Bmatrix}, \quad (20)$$

where  $\Delta z_k = z_{k+1} - z_k$ , and, e.g., if  $\hat{\phi}_1^{i,j,k} = \hat{\phi}_1(x, y, z)$  then  $\hat{\phi}_1^{i+1,j,k} = \hat{\phi}_1(x + \Delta x, y, z)$ .

Since the random fields are filtered such that the variance of  $\hat{\boldsymbol{\phi}}$  remains unity everywhere, then, given that the three fields  $\hat{\phi}_1, \hat{\phi}_2$  and  $\hat{\phi}_3$  are uncorrelated with each other, the three variance components of the acceleration field at a particular grid level  $k$  are given by

$$(\sigma_{a_i}^2)_k = \begin{cases} \frac{2g_k^2}{\Delta y^2}(1 - \rho_k^{\Delta y}) + \frac{1}{\Delta z_k^2}(g_{k+1}^2 + g_k^2 - 2g_{k+1}g_k\rho_k^{\Delta z_k}), & i = 1 \\ \frac{1}{\Delta z_k^2}(g_{k+1}^2 + g_k^2 - 2g_{k+1}g_k\rho_k^{\Delta z_k}) + \frac{2g_k^2}{\Delta x^2}(1 - \rho_k^{\Delta x}), & i = 2 \\ \frac{2g_k^2}{\Delta x^2}(1 - \rho_k^{\Delta x}) + \frac{2g_k^2}{\Delta y^2}(1 - \rho_k^{\Delta y}), & i = 3 \end{cases} \quad (21)$$

where, e.g.,  $\rho_k^{\Delta x}$  denotes the autocorrelation coefficient between  $\hat{\phi}(x, y, z)$  and  $\hat{\phi}(x + \Delta x, y, z)$  for any of  $\hat{\phi}_1, \hat{\phi}_2$  or  $\hat{\phi}_3$  at grid level  $k$ . These autocorrelations will take a value between 0 and 1 depending on the chosen filtering procedure. For example, with the MT92 model, a 1:2:1 filter is applied to random numbers generated directly on the model grid, and it can be shown that  $\rho^{\Delta x} = \rho^{\Delta y} = \rho^{\Delta z} = 2/3$  at every grid level. Similarly, with the WM08 model, a 1:4:6:4:1 filter (equivalent to a double application of the 1:2:1 filter) is applied to random numbers generated on an isotropic grid, and we have  $\rho^{\Delta x} = \rho^{\Delta y} = \rho^{\Delta z} = 4/5$  at every isotropic grid level (the values after interpolation onto the anisotropic model grid may also be derived, but this is not shown here for brevity). The autocorrelations expected with the new GAF model are given by Eq. (17).

Finally, combining Eqs. (13) and (21) then leads to a quadratic equation for  $g_k$  with solutions

$$g_k = \frac{-b \pm \sqrt{b^2 - 4ac}}{2a}, \quad \text{where} \quad (22)$$

$$a = \frac{4}{\Delta x^2} (1 - \rho_k^{\Delta x}) + \frac{4}{\Delta y^2} (1 - \rho_k^{\Delta y}) + \frac{2}{\Delta z_k^2},$$

$$b = \frac{-4g_{k+1}\rho_k^{\Delta z_k}}{\Delta z_k^2}, \quad c = \frac{2g_{k+1}^2}{\Delta z_k^2} - \frac{2C_B}{T_B} \left(\frac{l_k}{l_0}\right)^5 \langle \epsilon \rangle_k$$

In practice, we must first calculate the scaling factor at the top grid level,  $g_n$  say, by assuming that  $g_{n+1} = g_n$ , but then proceed down the grid levels using the full quadratic Eq. (22) and taking the larger root (positive sign) when real solutions exist.

## B2. Derivation of the point-wise scaling factor, $g_{i,j,k}$

For the point-wise scaling factor, we have that  $\phi^{i,j,k} = g_{i,j,k} \hat{\phi}^{i,j,k}$ . Assuming that local gradients in the scaling factor are small, i.e. that  $\Delta g_{i,j,k} \ll g_{i,j,k}$  in all 3 dimensions, where  $\Delta g_{i,j,k}$  is the difference between  $g_{i,j,k}$  and the scaling factor at the adjacent grid point in the positive direction of a given dimension, leads to the following set of equations for the point-wise backscatter acceleration variance components:

$$(\sigma_{a_m}^2)_{i,j,k} = \begin{cases} \frac{2g_{i,j,k}^2}{\Delta y_j^2} (1 - \rho_{i,j,k}^{\Delta y_j}) + \frac{2g_{i,j,k}^2}{\Delta z_k^2} (1 - \rho_{i,j,k}^{\Delta z_k}), & m = 1 \\ \frac{2g_{i,j,k}^2}{\Delta z_k^2} (1 - \rho_{i,j,k}^{\Delta z_k}) + \frac{2g_{i,j,k}^2}{\Delta x_i^2} (1 - \rho_{i,j,k}^{\Delta x_i}), & m = 2 \\ \frac{2g_{i,j,k}^2}{\Delta x_i^2} (1 - \rho_{i,j,k}^{\Delta x_i}) + \frac{2g_{i,j,k}^2}{\Delta y_j^2} (1 - \rho_{i,j,k}^{\Delta y_j}), & m = 3 \end{cases} \quad (23)$$

Combining Eqs. (4) and (23) then leads to:

$$g_{i,j,k} = \sqrt{\frac{\frac{2C_B}{T_B} \left(\frac{l_k}{l_0}\right)^5 \epsilon_{i,j,k}}{\frac{4}{\Delta x_i^2} (1 - \rho_{i,j,k}^{\Delta x_i}) + \frac{4}{\Delta y_j^2} (1 - \rho_{i,j,k}^{\Delta y_j}) + \frac{4}{\Delta z_k^2} (1 - \rho_{i,j,k}^{\Delta z_k})}} \quad (24)$$

## References

- Brasseur JG, Wei T. 2010. Designing large-eddy simulation of the turbulent boundary layer to capture law-of-the-wall scaling. *Physics of Fluids*. 22. DOI: 10.1063/1.3319073
- Businger JA, Wyngaard JC, Izumi Y, Bradley EF. 1971. Flux-Profile Relationships in the Atmospheric Surface Layer. *Journal of the Atmospheric Sciences*. 28: 181-189. DOI: 10.1175/1520-0469(1971)028<0181:fprita>2.0.co;2
- Cai XM. 1999. Large-eddy simulation of the convective boundary layer over an idealized patchy urban surface. *Quarterly Journal of the Royal Meteorological Society*. 125: 1427-1444. DOI: 10.1256/smsqj.55615
- Chamecki M. 2010. Modeling subgrid-scale heat fluxes in the neutral and stratified atmospheric boundary layer. *Journal of Turbulence*. 11: 1-16. DOI: 10.1080/14685241003785881
- Chasnov JR. 1991. Simulation of the Kolmogorov inertial subrange using an improved subgrid model. *Physics of Fluids A-Fluid Dynamics*. 3: 188-200. DOI: 10.1063/1.857878

- Chow FK, Street RL, Xue M, Ferziger JH. 2005. Explicit filtering and reconstruction turbulence modeling for large-eddy simulation of neutral boundary layer flow. *Journal of the Atmospheric Sciences*. 62: 2058-2077. DOI: 10.1175/jas3456.1
- Deardorff JW. 1970. A numerical study of three-dimensional turbulent channel flow at large Reynolds numbers. *Journal of Fluid Mechanics*. 41: 453-480
- Domaradzki JA, Saiki EM. 1997. Backscatter models for large-eddy simulations. *Theoretical and Computational Fluid Dynamics*. 9: 75-83. DOI: 10.1007/s001620050033
- Frederiksen JS, Davies AG. 1997. Eddy viscosity and stochastic backscatter parameterizations on the sphere for atmospheric circulation models. *Journal of the Atmospheric Sciences*. 54: 2475-2492. DOI: 10.1175/1520-0469(1997)054<2475:evasbp>2.0.co;2
- Garratt JR. 1994. *The atmospheric boundary layer*. Cambridge University Press: Cambridge, UK.
- Germano M, Piomelli U, Moin P, Cabot WH. 1991. A dynamic subgrid-scale eddy viscosity model. *Physics of Fluids A-Fluid Dynamics*. 3: 1760-1765. DOI: 10.1063/1.857955
- Geurts BJ. 2004. *Elements of direct and large-eddy simulation*. R.T. Edwards: Philadelphia, USA.
- Grant ALM. 1986. Observations of boundary layer structure made during the 1981 KONTUR experiment. *Quarterly Journal of the Royal Meteorological Society*. 112: 825-841. DOI: 10.1002/qj.49711247314
- Kaimal JC, Wyngaard JC, Izumi Y, Coté R. 1972. Spectral characteristics of surface-layer turbulence. *Quarterly Journal of the Royal Meteorological Society*. 98: 563-589. DOI: 10.1002/qj.49709841707
- Kirkil G, Mirocha J, Bou-Zeid E, Chow FK, Kosovic B. 2012. Implementation and Evaluation of Dynamic Subfilter-Scale Stress Models for Large-Eddy Simulation Using WRF. *Monthly Weather Review*. 140: 266-284. DOI: 10.1175/mwr-d-11-00037.1
- Kosovic B. 1997. Subgrid-scale modelling for the large-eddy simulation of high-Reynolds-number boundary layers. *Journal of Fluid Mechanics*. 336: 151-182. DOI: 10.1017/s0022112096004697
- Kravchenko AG, Moin P, Moser R. 1996. Zonal Embedded Grids for Numerical Simulations of Wall-Bounded Turbulent Flows. *Journal of Computational Physics*. 127: 412-423. DOI: 10.1006/jcph.1996.0184
- Leith CE. 1990. Stochastic backscatter in a subgrid-scale model - plane shear mixing layer. *Physics of Fluids A-Fluid Dynamics*. 2: 297-299. DOI: 10.1063/1.857779
- Leslie DC, Quarini GL. 1979. Application of turbulence theory to the formulation of sub-grid modeling procedures. *Journal of Fluid Mechanics*. 91: 65-91. DOI: 10.1017/s0022112079000045
- Lu H, Porté-Agel F. 2014. On the Development of a Dynamic Non-linear Closure for Large-Eddy Simulation of the Atmospheric Boundary Layer. *Boundary-Layer Meteorology*. 151: 429-451. DOI: 10.1007/s10546-013-9906-y
- Mason PJ. 1994. Large-eddy simulation - A critical-review of the technique. *Quarterly Journal of the Royal Meteorological Society*. 120: 1-26. DOI: 10.1002/qj.49712051503
- Mason PJ, Brown AR. 1994. The sensitivity of large-eddy simulation of turbulent shear flow to subgrid models. *Boundary-Layer Meteorology*. 70: 133-150. DOI: 10.1007/bf00712526
- Mason PJ, Thomson DJ. 1992. Stochastic backscatter in large-eddy simulations of boundary-layers. *Journal of Fluid Mechanics*. 242: 51-78. DOI: 10.1017/s0022112092002271

- Michioka T, Chow FK. 2008. High-Resolution Large-Eddy Simulations of Scalar Transport in Atmospheric Boundary Layer Flow over Complex Terrain. *Journal of Applied Meteorology and Climatology*. 47: 3150-3169. DOI: 10.1175/2008jamc1941.1
- Mirocha J, Kirkil G, Bou-Zeid E, Chow FK, Kosović B. 2012. Transition and Equilibration of Neutral Atmospheric Boundary Layer Flow in One-Way Nested Large-Eddy Simulations Using the Weather Research and Forecasting Model. *Monthly Weather Review*. 141: 918-940. DOI: 10.1175/mwr-d-11-00263.1
- Mirocha JD, Lundquist JK, Kosovic B. 2010. Implementation of a Nonlinear Subfilter Turbulence Stress Model for Large-Eddy Simulation in the Advanced Research WRF Model. *Monthly Weather Review*. 138: 4212-4228. DOI: 10.1175/2010mwr3286.1
- Palmer T, Buizza R, Doblas-Reyes F, Jung T, Leutbecher M, Shutts G, Steinheimer M, Weisheimer A. 2009. *Stochastic parametrization and model uncertainty*. European Centre for Medium-Range Weather Forecasts: Reading, UK.
- Piomelli U, Kang S, Ham F, Iaccarino G. 2006. Effect of discontinuous filter width in large-eddy simulations of plane channel flow. *Center for Turbulence Research, Proceedings of the Summer Program 2006*. 151-162
- Schumann U. 1995. Stochastic backscatter of turbulence energy and scalar variance by random subgrid-scale fluxes. *Proceedings of the Royal Society-Mathematical and Physical Sciences*. 451: 293-318. DOI: 10.1098/rspa.1995.0126
- Shutts G. 2005. A kinetic energy backscatter algorithm for use in ensemble prediction systems. *Quarterly Journal of the Royal Meteorological Society*. 131: 3079-3102. DOI: 10.1256/qj.04.106
- Smagorinsky J. 1963. General circulation experiments with the primitive equations. *Monthly Weather Review*. 91: 99-164. DOI: 10.1175/1520-0493(1963)091<0099:gcewtp>2.3.co;2
- Sullivan PP, Horst TW, Lenschow DH, Moeng CH, Weil JC. 2003. Structure of subfilter-scale fluxes in the atmospheric surface layer with application to large-eddy simulation modelling. *Journal of Fluid Mechanics*. 482: 101-139. DOI: 10.1017/s0022112003004099
- Sullivan PP, McWilliams JC, Moeng CH. 1994. A subgrid-scale model for large-eddy simulation of planetary boundary-layer flows. *Boundary-Layer Meteorology*. 71: 247-276. DOI: 10.1007/bf00713741
- Talbot C, Bou-Zeid E, Smith J. 2012. Nested Mesoscale Large-Eddy Simulations with WRF: Performance in Real Test Cases. *Journal of Hydrometeorology*. 13: 1421-1441. DOI: 10.1175/jhm-d-11-048.1
- Vanella M, Piomelli U, Balaras E. 2008. Effect of grid discontinuities on large-eddy simulation statistics and flow fields. *Journal of Turbulence*. 9: 1-23. DOI: 10.1080/14685240802446737
- Von Kármán T. 1931. *Mechanical similitude and turbulence*. National Advisory Committee for Aeronautics: Washington, USA.
- Weinbrecht S, Mason PJ. 2008. Stochastic backscatter for cloud-resolving models. Part I: Implementation and testing in a dry convective boundary layer. *Journal of the Atmospheric Sciences*. 65: 123-139. DOI: 10.1175/2007jas2166.1
- Westbury PS, Dunn DC, Morrison JF. 2004. Analysis of a stochastic backscatter model for the large-eddy simulation of wall-bounded flow. *European Journal of Mechanics B-Fluids*. 23: 737-758. DOI: 10.1016/j.euromechflu.2004.01.003
- Wirjadi O, Breuel T. Approximate separable 3D anisotropic Gauss filter. *Image Processing, IEEE International Conference, 11-14 September 2005*. DOI: 10.1109/ICIP.2005.1530013



Zidikheri MJ, Frederiksen JS. 2009. Stochastic Subgrid Parameterizations for Simulations of Atmospheric Baroclinic Flows. *Journal of the Atmospheric Sciences*. 66: 2844-2858. DOI: 10.1175/2009jas3036.1

**Table I – The LES model grids.**

<b>Grid</b>	<b><math>\Delta x</math> (m)</b>	<b><math>\Delta y</math> (m)</b>	<b><math>Nx</math></b>	<b><math>Ny</math></b>	<b><math>\Delta z_1</math> (m)</b>	<b><math>\Delta x/\Delta z_1</math></b>	<b><math>S_{\Delta z}</math></b>	<b><math>\Delta z_{\max}</math> (m)</b>	<b><math>Nz</math></b>
<b>G1</b>	50	50	64	64	50	1	1.03	50	128
<b>G2</b>	50	50	64	64	25	2	1.03	50	99
<b>G3</b>	50	50	64	64	10	5	1.03	50	79
<b>G4</b>	50	50	64	64	5	10	1.03	50	58

**Table II – The SGS models.**

<b>Model</b>	<b>Reference</b>	<b>Filter</b>	<b><math>n</math></b>	<b><math>C_B</math></b>	<b><math>T_B</math></b>	<b><math>z_{B_{\max}}</math></b>
<b>SMAG</b>	Smagorinsky (1963)	-	-	-	-	-
<b>GAF</b>	-	Equation (8) with $\lambda = 1$	4	0.6	$2\Delta t$	500 m
<b>MT92</b>	Mason and Thomson (1992)	3-D 1: 4: 6: 4: 1	4	0.6	$2\Delta t$	500 m
<b>WM08</b>	Weinbrecht and Mason (2008)	3-D 1: 4: 6: 4: 1	4	0.6	$2\Delta t$	500 m

**Figure 1 – Schematic showing the characteristic length scale and anisotropy of backscatter acceleration fields generated using (a) the MT92 model, (b) the WM08 model, and (c) the proposed new model. Unphysical inconsistencies are noted in *italic font*. See main text for more details.**

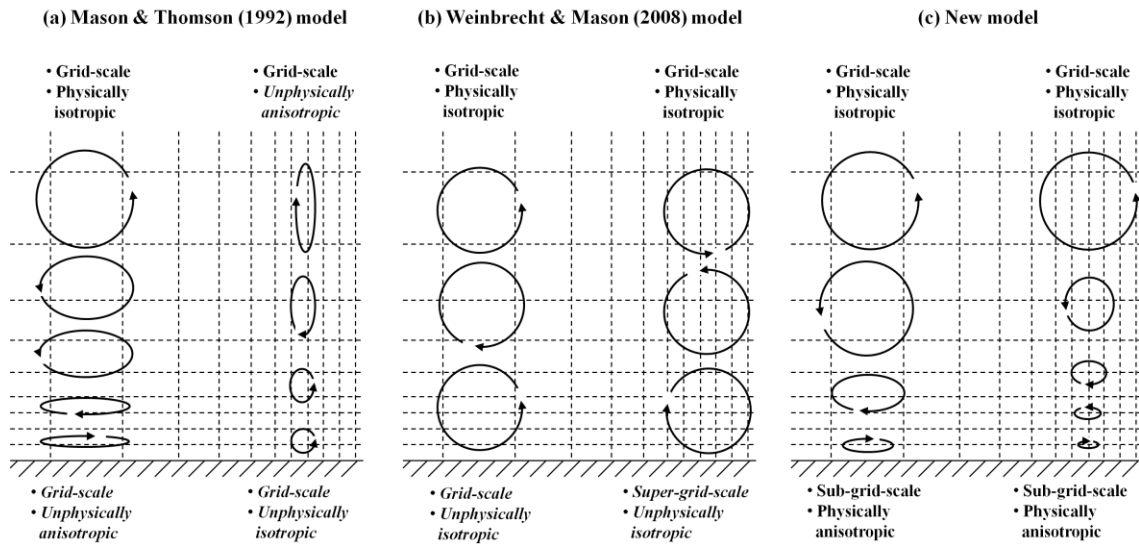


Figure 2 – Weights,  $W$ , of the discrete grid-adaptive Gaussian filter in the  $z$ -dimension, for  $l_B = 0.8\Delta x$  and  $\sigma_{a_1}^2 : \sigma_{a_2}^2 : \sigma_{a_3}^2 = 1 : 1 : 1$ , when (a) the filter is centred on a grid point at  $z = z_f$ , for four separate grids with  $\alpha = \Delta x/\Delta z = 1, 2, 4$  and  $8$ , respectively; and (b) the filter is centred on 3 separate grid points (shown by inner tick marks on the lower axis) on a stretched vertical grid (shown by outer tick marks on the lower axis).

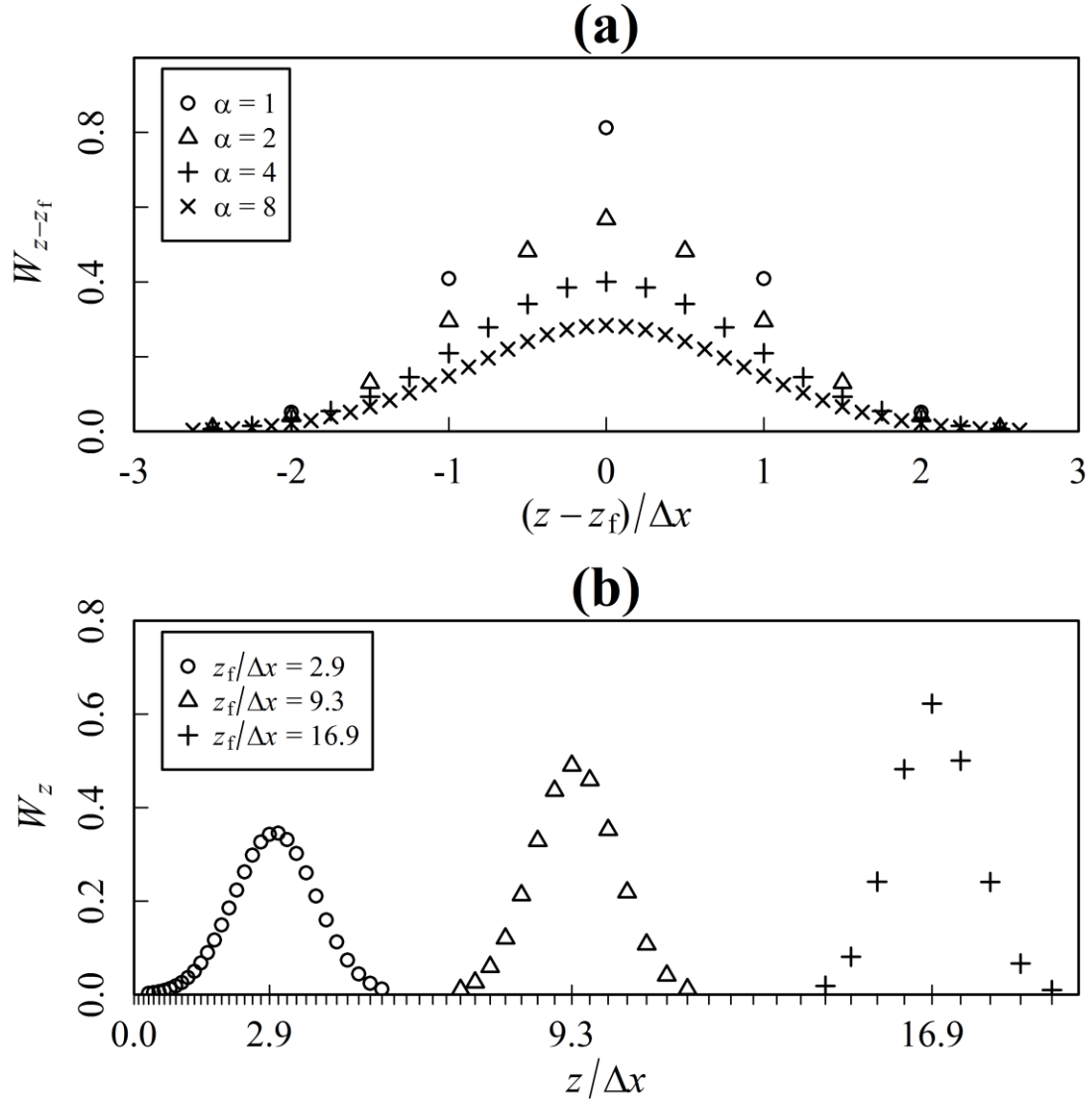
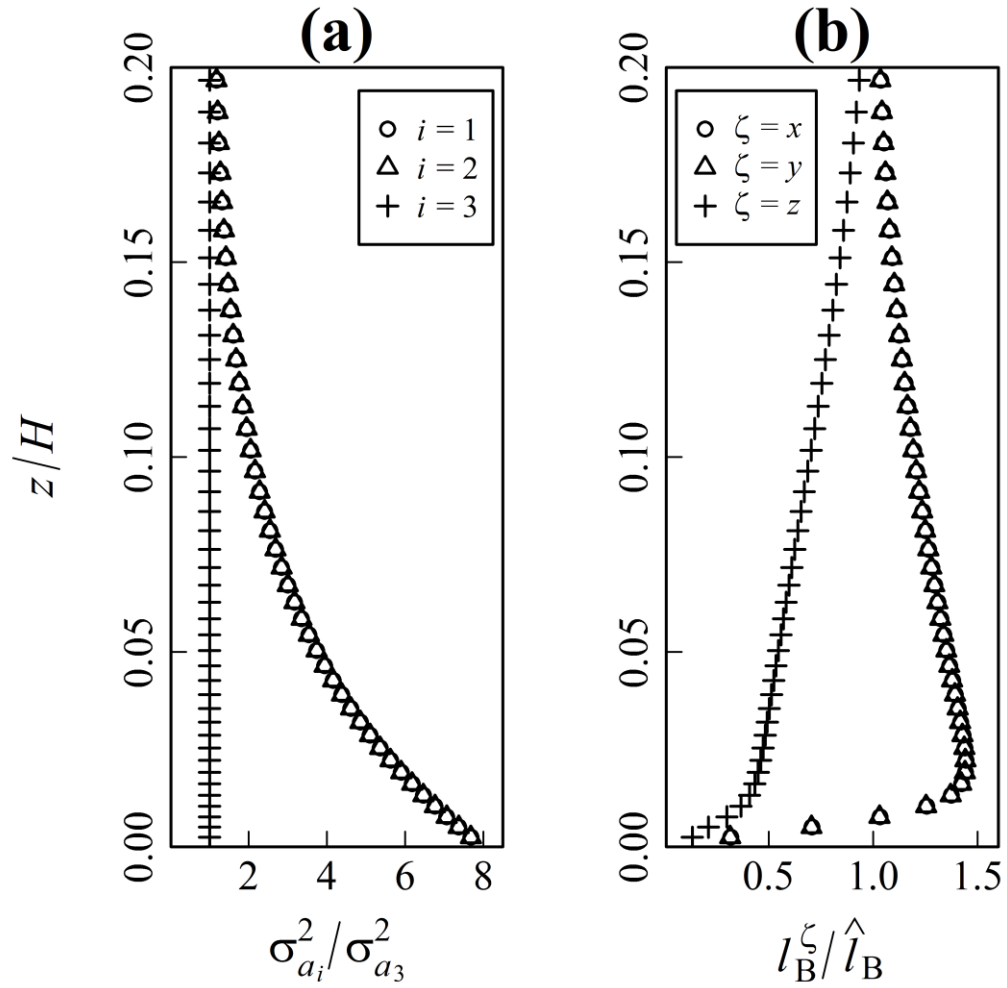


Figure 3 – For the GAF model, (a) the imposed anisotropy in the backscatter acceleration fields, as shown by the acceleration variance ratio profiles; (b) the resulting profiles, on grid G4, of the backscatter length scale components,  $l_B^\zeta$ , normalised by the backscatter length scale in the flow interior,  $\hat{l}_B$ .



**Figure 4 – Surface-layer contour plots through backscatter acceleration fields generated using each backscatter model: (a) MT92, (b) WM08, (c) GAF, on grid G4 (horizontal and vertical grid spacing is shown by outer tick marks on left and upper axes, respectively). Each field shows acceleration magnitudes and is normalised by its maximum value.**

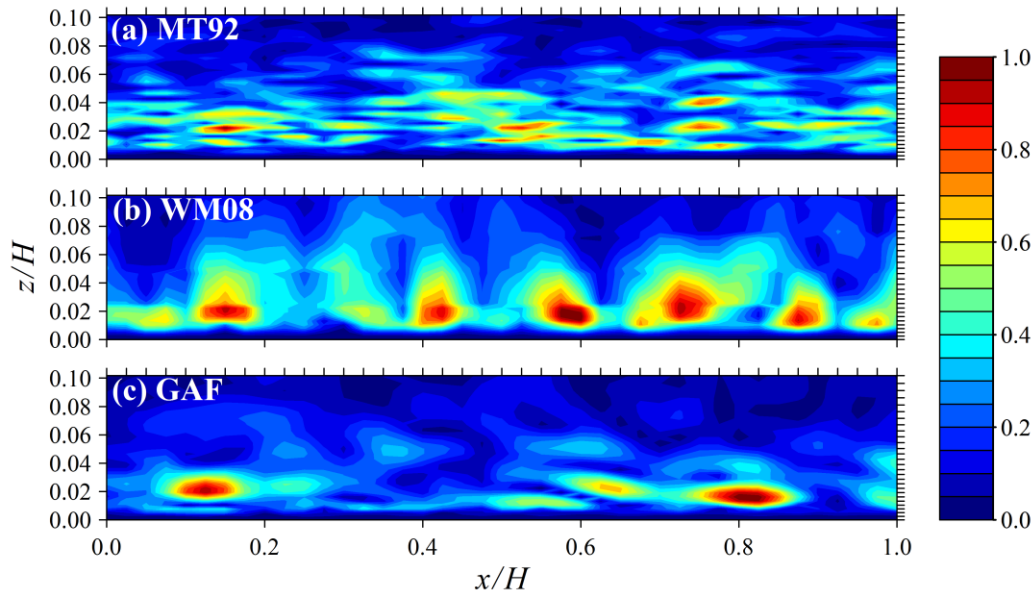
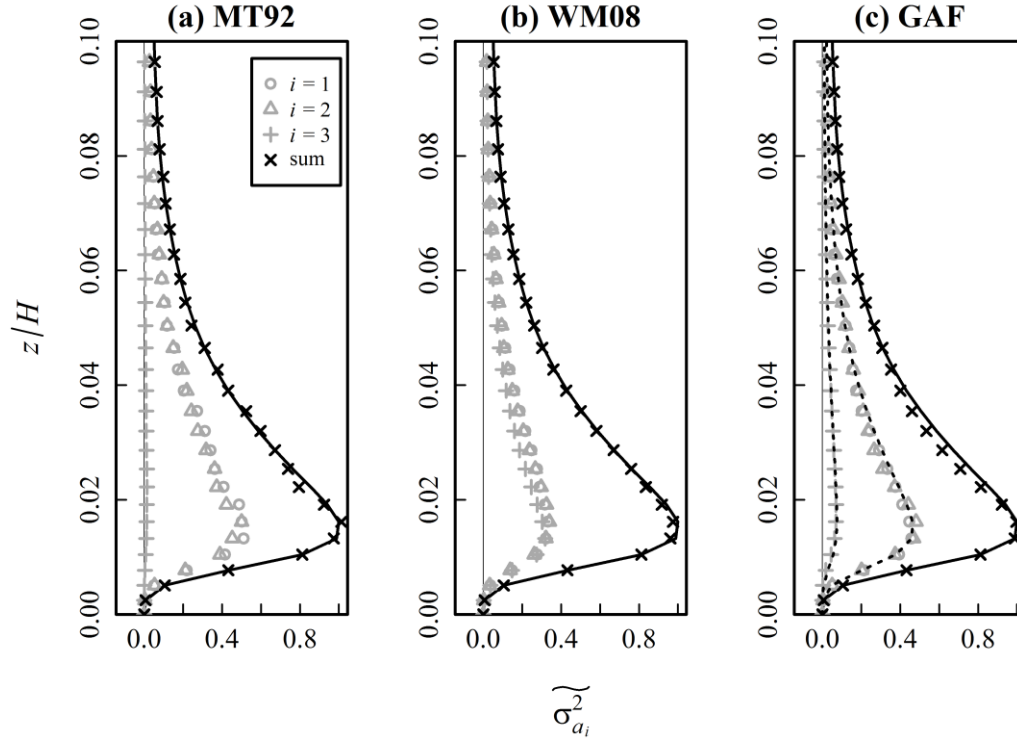


Figure 5 - Surface-layer profiles of the three variance components, and their sum, for the three backscatter acceleration fields shown in Figure 4 for the (a) MT92, (b) WM08, and (c) GAF model. Solid line shows the target backscatter variance profile as given by the right hand side of Eq. (13). All values are normalised by the maximum of the target profile. For the GAF model, dashed lines show the expected variance profiles resulting from the imposed backscatter anisotropy (see Figure 3(a)).





**Figure 6 - Surface-layer profiles of normalised root-mean-square (RMS) grid-cell divergences for the three backscatter acceleration fields shown in Figure 4 for the (a) MT92, (b) WM08, and (c) GAF model. See text for more details.**

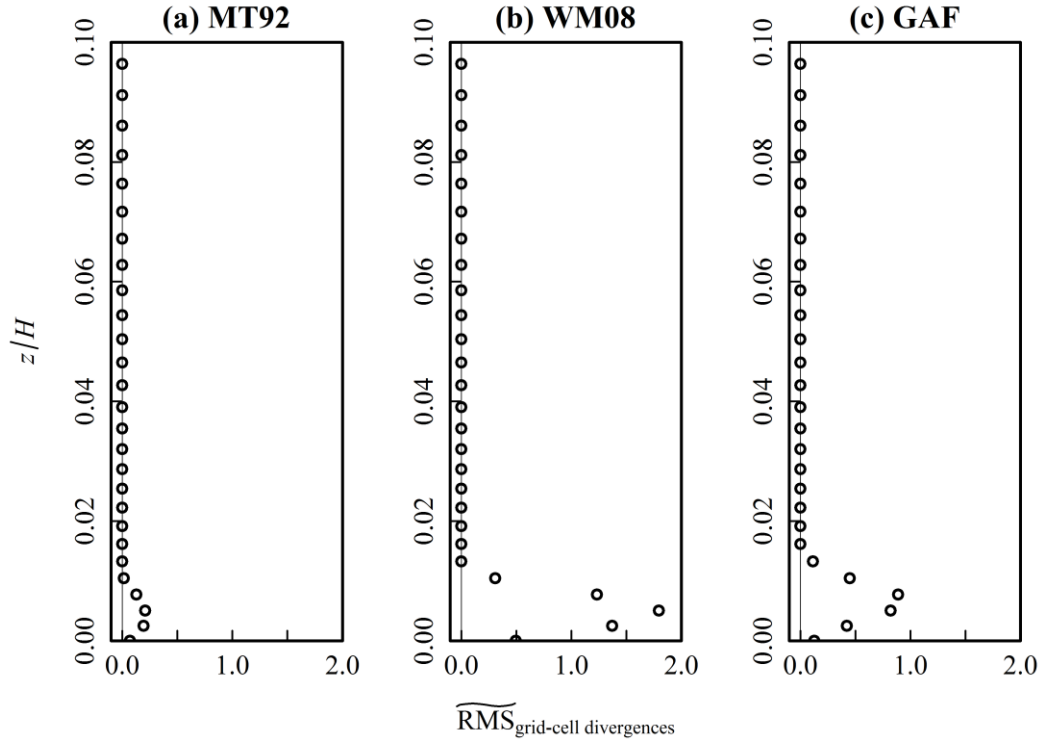
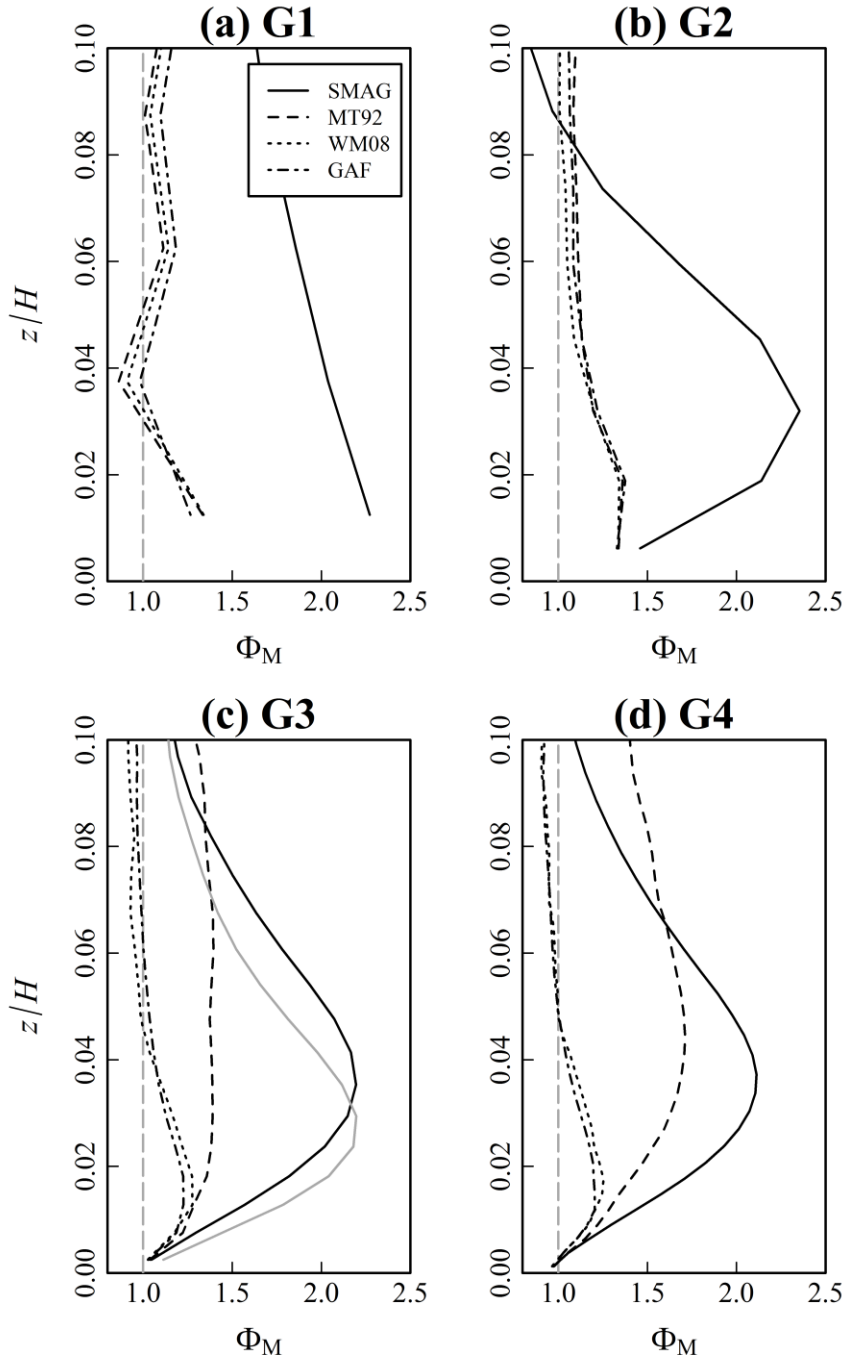


Figure 7 – Surface-layer profiles of mean nondimensional velocity shear,  $\Phi_M$ , obtained with each SGS model, for each model grid: (a) G1, (b) G2, (c) G3, and (d) G4. The grey dashed lines through  $\Phi_M = 1$  corresponds to the theoretical profile for a neutral surface layer. The lowest grid point is set by the surface boundary condition and so is not plotted. The solid grey line in panel (c) shows the profile obtained with the SMAG model when the grid resolution is increased such that the additional required CPU time is similar to that required for the backscatter models.



**Figure 8 – LES time series (thin lines) and fitted exponential trend-lines (thick lines) of maximum nondimensional velocity shear,  $S$ , within the surface layer, after each backscatter model (Mt92, WM08, GAF) is activated from an initially quasi-steady state without backscatter (SMAG), on grid G3.**

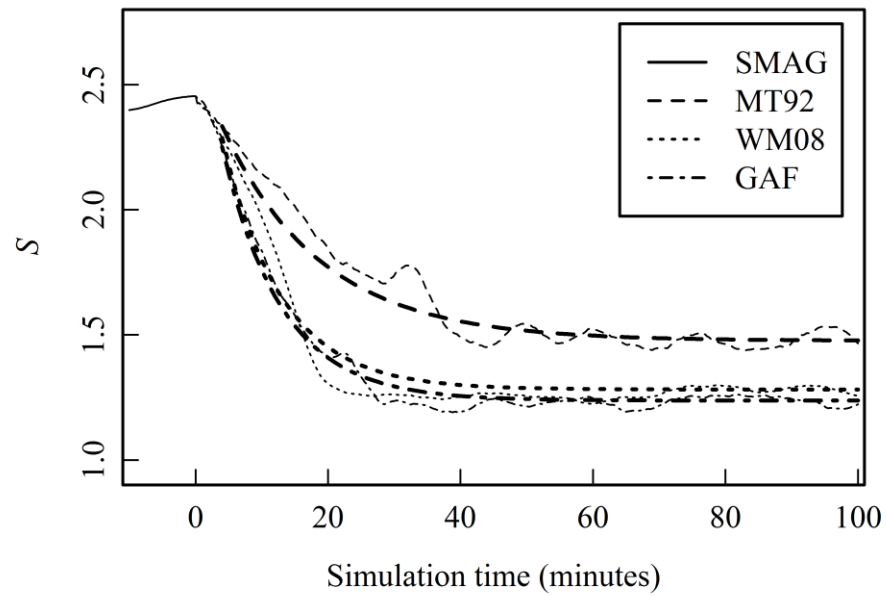


Figure 9 – Near-surface profiles of resolved velocity variances,  $\sigma_u^2$ ,  $\sigma_v^2$  and  $\sigma_w^2$ , obtained with each SGS model: (a) SMAG, (b) MT92, (c) WM08, and (d) GAF, on grid G4.

